Cell

Article

Discovery of a Regulatory Subunit of the Yeast Fatty Acid Synthase

Graphical Abstract

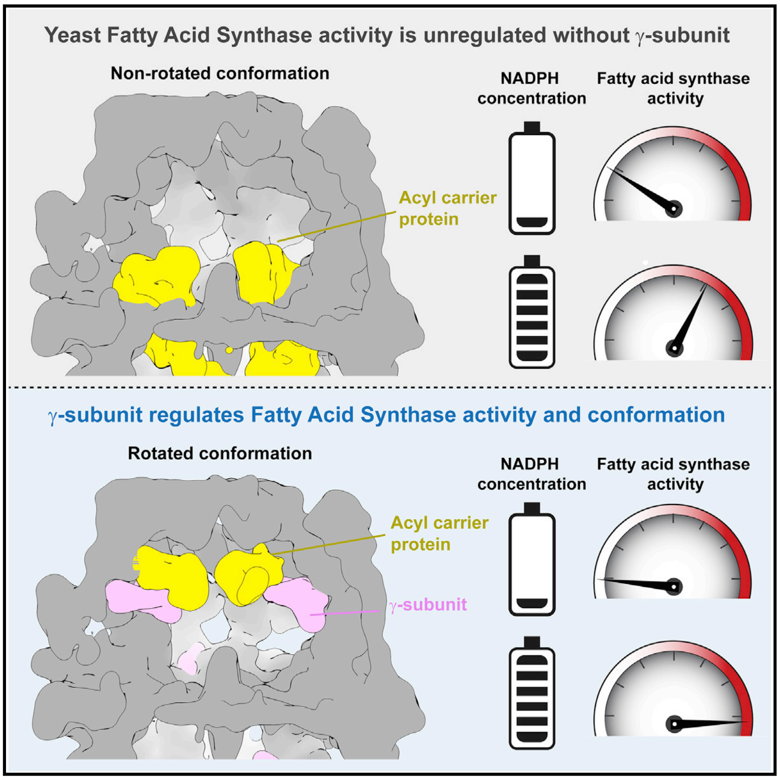

Highlights

- Discovery of a regulatory γ subunit of the yeast fatty acid synthase (FAS)
- The γ subunit regulates FAS reductase activities by kinetic hysteresis
- Establishes structural basis for γ subunit-mediated FAS activity regulation
- The γ subunit defines a higher efficiency FAS functional compartment

Authors

Kashish Singh, Benjamin Graf, Andreas Linden, ..., Kai Tittmann, Holger Stark, Ashwin Chari

Correspondence

holger.stark@mpibpc.mpg.de (H.S.),
ashwin.chari@mpibpc.mpg.de (A.C.)

In Brief

Structural analysis identifies a new regulator of yeast fatty acid synthase.

Singh et al., 2020, Cell *180*, 1130–1143
March 19, 2020 © 2020 Elsevier Inc.
https://doi.org/10.1016/j.cell.2020.02.034

CellPress

Cell

Article

Discovery of a Regulatory Subunit of the Yeast Fatty Acid Synthase

Kashish Singh,[1,5] Benjamin Graf,[1,5] Andreas Linden,[2,3] Viktor Sautner,[1,4] Henning Urlaub,[2,3] Kai Tittmann,[1,4]
Holger Stark,[1,*] and Ashwin Chari[1,6,*]
[1]Department of Structural Dynamics, Max Planck Institute for Biophysical Chemistry, 37077 Göttingen, Germany
[2]Bioanalytical Mass Spectrometry, Max Planck Institute for Biophysical Chemistry, 37077 Göttingen, Germany
[3]University Medical Center Göttingen, Institute of Clinical Chemistry, Bioanalytics, 37075 Göttingen, Germany
[4]Göttinger Zentrum für Molekulare Biowissenschaften and Schwann-Schleiden-Forschungszentrum, Georg-August-Universität Göttingen, 37077 Göttingen, Germany
[5]These authors contributed equally
[6]Lead Contact
*Correspondence: holger.stark@mpibpc.mpg.de (H.S.), ashwin.chari@mpibpc.mpg.de (A.C.)
https://doi.org/10.1016/j.cell.2020.02.034

SUMMARY

Fatty acid synthases (FASs) are central to metabolism but are also of biotechnological interest for the production of fine chemicals and biofuels from renewable resources. During fatty acid synthesis, the growing fatty acid chain is thought to be shuttled by the dynamic acyl carrier protein domain to several enzyme active sites. Here, we report the discovery of a γ subunit of the 2.6 megadalton α_6-β_6 *S. cerevisiae* FAS, which is shown by high-resolution structures to stabilize a rotated FAS conformation and rearrange ACP domains from equatorial to axial positions. The γ subunit spans the length of the FAS inner cavity, impeding reductase activities of FAS, regulating NADPH turnover by kinetic hysteresis at the ketoreductase, and suppressing off-pathway reactions at the enoylreductase. The γ subunit delineates the functional compartment within FAS. As a scaffold, it may be exploited to incorporate natural and designed enzymatic activities that are not present in natural FAS.

INTRODUCTION

Fatty acids and their biosynthesis are essential for the survival of all organisms, representing building blocks of biological membranes, but also energy reserves of a cell and precursors to second messenger molecules (Graber et al., 1994). In bacteria, yeasts, and plants, the *de novo* biosynthesis of fatty acids is essential for survival (Schweizer and Hofmann, 2004; White et al., 2005), while metazoans rely on additional dietary uptake (Burr and Brown, 1933). Subtle changes in fatty acid synthesis impact numerous vital cellular functions and are thus linked to ailments like cancer and obesity (López et al., 2007; Ronnett et al., 2006; Wang and Dubois, 2012).

In light of the central metabolic role of fatty acid synthesis, a common biosynthetic route is employed by all organisms (Figure 1A), necessitating four central metabolites—acetyl-CoA, malonyl-CoA, NAD(P)H, and ATP. Despite conservation of the biosynthetic reaction mechanisms, the architecture of fatty acid synthase (FAS) differs across the kingdoms of life. Plants, bacteria, and mitochondria harbor the required activities on individual polypeptides (type II FAS) (White et al., 2005). Type I FAS systems, where the synthetic activities are combined within a single macromolecular complex, are found in yeasts, Corynebacteria/Mycobacteria/Nocardia (CMN) group bacteria, as well as in higher eukaryotes (Schweizer and Hofmann, 2004). In higher eukaryotes, FAS is formed by a cross-shaped homodimer (Maier et al., 2008; Smith et al., 2003). Structural studies by multiple labs have established that the type I fungal FAS is a D3 symmetric 2.6 MDa multi-enzyme complex that forms a barrel-shaped particle with a length of 270 Å and a width of 250 Å (Gipson et al., 2010; Jenni et al., 2007; Leibundgut et al., 2007; Lomakin et al., 2007; Stoops and Wakil, 1978; Wieland et al., 1978). These studies indicate that the *S. cerevisiae* FAS is composed of six α subunit copies, which form an equatorial central wheel, and six β subunit copies, which form the two domes of the particle (Figure 1B). All enzymatic activities required for the synthesis of saturated C_{16}-C_{18} fatty acid chains reside within α- and β-subunits (Figure 1C) (Lynen, 1980; Schweizer and Hofmann, 2004). The α-subunit contains ketoreductase (KR), ketosynthase (KS), and phosphopantetheine transferase (PPT) domains, while the β subunit harbors acetyltransferase (AT), enoylreductase (ER), and dehydratase (DH) domains. The malonyl/palmitoyl transferase (MPT) domain is mostly formed by the C-terminal part of the β subunit and completed by the N terminus of the α subunit (Jenni et al., 2007; Leibundgut et al., 2007). The acyl carrier protein (ACP) domain is tethered flexibly onto the α subunit (Gipson et al., 2010; Leibundgut et al., 2007; Lomakin et al., 2007) and its movement is restricted by spatial confinement within the dome. ACP-bound intermediates are thought to be iteratively shuttled to all active sites in a stochastic manner (Anselmi et al., 2010; Leibundgut et al., 2007), similar to the multiple random coupling mechanism proposed for other multi-enzyme complexes (Prajapati et al., 2019). In addition to academic interest in fatty acid biosynthesis, fatty acids have emerged as platform compounds for the biotechnological production of fine chemicals and biofuels (Biermann et al., 2011; Marella et al., 2018; Yu et al., 2014; Zhou et al.,

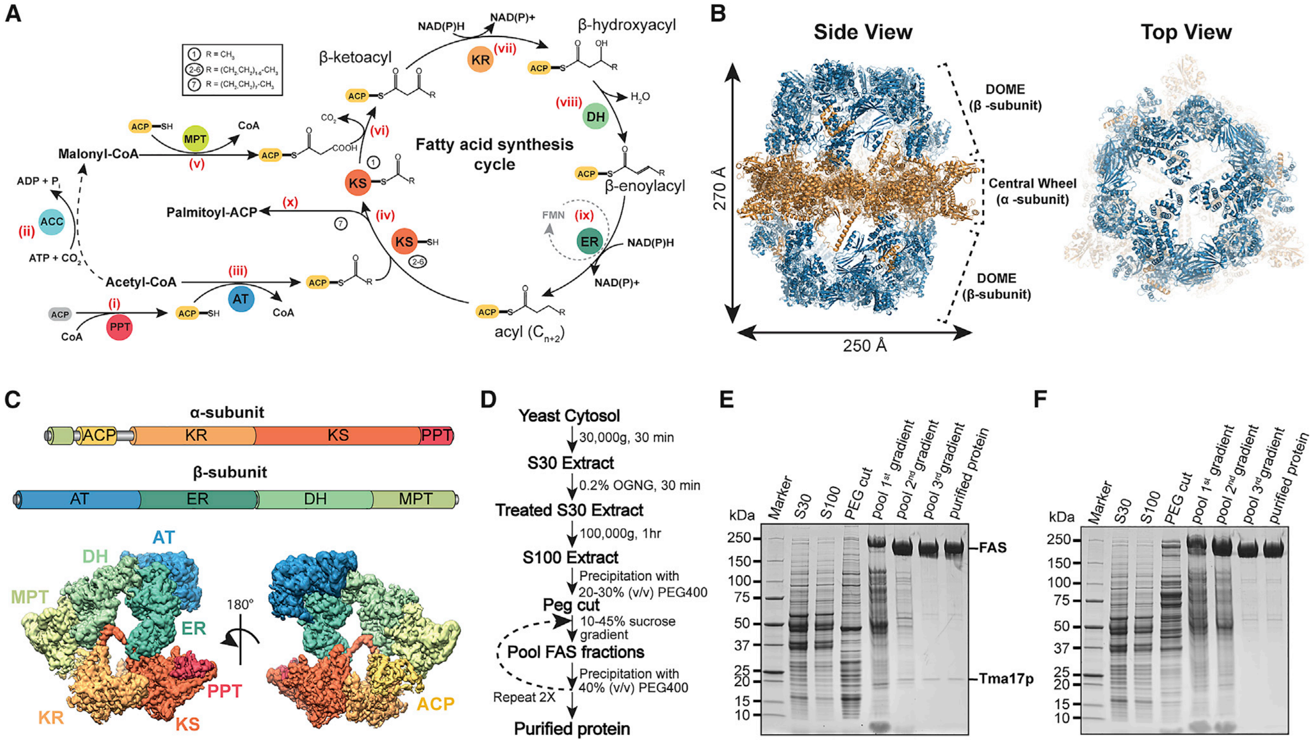

Figure 1. Discovery of Tma17p as a FAS Binding Protein

(A) General catalytic cycle of fatty acid biosynthesis, which is an iterative process and requires the activation of acyl carrier protein (ACP) by the phosphopantetheine transferase (PPT; i). Malonyl-CoA is synthesized from acetyl-CoA and CO_2 by acetyl-CoA carboxylase (ACC; ii). The first two carbon atoms of the fatty acid chain originating from acetyl-CoA (iii) are elongated using malonyl-CoA (v) through sequential ketosynthase (KS; iv and vi), ketoreductase (KR; vii), dehydratase (DH; viii), and enoylreductase (ER; harbors FMN in yeasts; ix) activities. The chain is elongated by two carbon atoms originating from malonyl-CoA in each cycle (i.e., 7 iterations are necessary to synthesize a 16-carbon chain).

(B) Overall architecture of the D3-symmetric yeast FAS. Six α-subunits (ochre) form a central wheel, three β-subunits (blue) each form the two domes of the barrel-like structure. The 2-fold axis dissects the central wheel perpendicularly, whereas the 3-fold axis runs down the length of the molecule, where the β-subunits join.

(C) Together, α- and β-subunits harbor all fatty acid biosynthetic activities: The ACP (yellow), KR (gold), KS (orange), and PPT (magenta) domains reside on the α-subunit, while AT (blue), ER (teal), and DH (green) reside on the β-subunit. The MPT (khaki) domain is built up both by α- and β-subunits.

(D) Schematic representation of the yeast FAS purification procedure used in this article (STAR Methods).

(E) SDS-PAGE of wild-type *S. cerevisiae* FAS purification. Aliquots of S30 (lane 2) and S100 (lane 3) extracts, the resuspended PEG cut (lane 4), the pool of the first, second, and third sucrose gradients (lanes 5, 6, and 7), as well as the finally purified protein (lane 7) and a molecular weight marker (lane 1) are depicted. Note the co-purification of a protein with an apparent molecular weight of 20 kDa.

(F) SDS-PAGE of FAS purification from the Δtma17 strain. Aliquots of the same fractions as in (E) are loaded. Note the absence of the protein band with an apparent molecular weight of 20 kDa.

2014). In this context, fungal FAS has been engineered to generate e.g., short chain fatty acids and related polyketides (Gajewski et al., 2017b, 2017a).

Despite academic and biotechnological interest in FAS, several mechanistic and regulatory aspects have remained elusive. The metabolic load exerted upon a cell for the biosynthesis of a single palmitic acid amounts to the energetic equivalent of 122 ATP molecules (Nelson and Cox, 2012). The energy consumption and central metabolic importance of FAS requires a tight control of its activity, which is ascribed to transcriptional control (Schweizer and Hofmann, 2004), through multiple layers of ACC regulation (Wakil et al., 1983) and feedback inhibition by palmitoyl- and stearoyl-CoA (Lust and Lynen, 1968). No protein that directly regulates FAS activity has been described to date. Equally, it is not known if stochastic ACP movement is coincident with conformational changes of fungal FAS domes, or if accessory factors are required, because FAS structures with ACPs in defined functional intermediate states remain elusive. Additionally, a functional unit within FAS is defined by spatial proximity of catalytic domains residing on α- and β-subunits in accordance with fungal FAS architecture (Anselmi et al., 2010; Leibundgut et al., 2007), but other possibilities cannot be excluded.

Here, we describe the discovery of a regulatory subunit of yeast FAS, which we propose to term the FAS γ subunit. A maximum of six γ subunit copies bind to a single $\alpha_6\beta_6$ FAS molecule occupying all six reaction chambers, with each γ subunit simultaneously contacting a single α subunit and two adjacent β subunits. γ subunit binding stabilizes a rotated FAS conformation, which is accompanied by ACP domains rearranging from KS domain positions to AT domain positions. The γ subunit regulates FAS enzymatic activity in response to the abundance of its co-substrate NADPH, induces hysteretic behavior of FAS turnover, and suppresses futile ER catalytic cycles. The γ subunit thus directly interacts with FAS, regulates its activity, and influences its structure, including the ACP shuttle system.

RESULTS

Discovery of a Yeast Fatty Acid Synthase Regulatory Subunit

To mechanistically interrogate structural determinants governing iterative shuttling, we set out to establish a purification procedure that would yield highly active, biochemically, and structurally homogeneous FAS from the yeast *S. cerevisiae*. We adapted a chromatography-free purification procedure to the FAS that had previously yielded preparations of higher specific activity for 20S and 26S proteasomes (Haselbach et al., 2017; Schrader et al., 2016). This approach relies on fractionated PEG precipitation and density gradient centrifugation as orthogonal purification steps (Figure 1D) and allows for gentle, yet stringent, purification at constant (low-) ionic strength (Figures 1D–1F). During the entire purification process, FAS concentrations never drop below 0.4 μM and we discovered a 20 kDa protein that reproducibly co-purifies with FAS (Figure 1E). Tandem-MS of tryptic digests identified this protein as Tma17p (Table S1). We cross-validated that Tma17p represents the co-purified 20 kDa protein by generating a Δtma17 knockout yeast strain and purifying FAS. As shown in Figure 1F, when purified from the Δtma17 strain, the 20 kDa band is absent from purified FAS fractions, corroborating the tandem-MS results. Thus, Tma17p co-purifies with the FAS and appears to represent a putative hitherto unknown subunit of yeast FAS.

Biochemical Characterization of the FAS-Tma17p Interaction

An additional protein subunit of yeast FAS has not been described in close to five decades of biochemical investigation. Tma17p has previously been described to be associated with the translational machinery or involved in proteasome assembly (Fleischer et al., 2006; Hanssum et al., 2014). However, SDS-PAGE and tandem-mass spectrometry (MS) analyses indicate that neither the ribosome nor the proteasome are present in stoichiometric amounts in our FAS preparations, whereas Tma17p definitively is (Figure 1E). Tma17p is widely conserved in yeasts (Figure S1A; Data S1) and has been described to be upregulated under conditions of cellular stress and function in the context of proteasome assembly (Hanssum et al., 2014; Rousseau and Bertolotti, 2016). However, we were unable to reproduce formerly described viability defects of Δtma17 yeast strains in response to stressors in several genetic backgrounds (Figure S1B). On the other hand, co-purification and co-sedimentation of Tma17p with FAS in the 40S region of gradients suggests a direct biochemical interaction, and Tma17p abundance in purified FAS fractions indicates that earlier copy number estimates are incorrect (https://www.yeastgenome.org) (Cherry et al., 2012).

Based on our results and widely contrasting earlier findings (Fleischer et al., 2006; Hanssum et al., 2014; Rousseau and Bertolotti, 2016), we chose to perform a series of control experiments to establish that Tma17p indeed is a bona fide subunit of yeast FAS. First, we investigated the stability of the Tma17p-FAS interaction in dependence of ionic strength. Purified FAS was loaded onto density gradients containing either 50 mM KCl, 150 mM KCl, or 250 mM KCl (Figure 2A). Co-purified, endogenous Tma17p quantitatively dissociates from FAS at 250 mM KCl, which results in the sedimentation of Tma17p in top fractions of density gradients, akin to recombinant Tma17p (rTma17p) (Figure S1C). At 150 mM KCl, roughly half of co-purified Tma17p dissociates, whereas at 50 mM KCl, the co-purified Tma17p remains firmly associated to FAS and co-sediments in the 40S region. Second, we asked if ΔTma17p-FAS could be reconstituted with rTma17p and if the stability of the reconstituted complex resembled that of the endogenous complex. While the reconstituted complex is stable at 50 mM KCl, rTma17p dissociates quantitatively at 150 mM KCl (Figure 2B). We attribute this difference to the lack of post-translational modification upon expression in *E. coli* (Table S1). Third, we set out to quantify the thermodynamics of Tma17p-binding to FAS. ΔTma17p-FAS was incubated with increasing amounts of recombinant, fluorescently labeled Tma17p, and complex formation was analyzed by native gel electrophoresis, followed by quantification of the FAS-bound Tma17p fluorescence. Binding of Tma17p to FAS results in the shift of its mobility to a position, where it co-migrates with FAS. When the experiment is performed at 1 μM FAS, full saturation occurs at a 6-fold molar excess of fluorescent Tma17p, indicating that 6 copies of Tma17p can simultaneously bind to one FAS molecule. When the binding data were fit with a sigmoidal binding model using the Hill equation, this experiment revealed a positive cooperativity of Tma17p binding to FAS (Hill coefficient of $n_H = 1.6 \pm 0.1$) and a dissociation constant of $K_{0.5} = 3.1 \pm 0.1$ μM (Figure 2C). When the data were alternatively fit with a quadratic equation, a $K_D = 0.35 \pm 0.07$ μM was obtained (Figure S1D). Fourth, fluorescently labeled trypsin inhibitor, which is both similar in size and charge, was unable to bind FAS under the same conditions (Figure S1E), negating unspecific binding of Tma17p to FAS. We asked if the entire Tma17p polypeptide segment is essential for its association with FAS. Guided by secondary structure predictions (Figure S1F), we either singly removed the N-terminal segment (1–24) or the C-terminal segment (117–150). Both deletions were individually sufficient to abolish binding of Tma17p to FAS (Figure 2D).

Taken together, these experiments indicate that Tma17p is a weakly associated, salt-labile, integral subunit of the yeast FAS. It appears to have escaped identification as a FAS subunit due to the relatively high salt conditions previously employed to purify FAS and spontaneous dissociation of Tma17p based on its weak affinity (Leibundgut et al., 2007; Lomakin et al., 2007). The observed cooperativity of binding and the synergistic requirement of both N as well as C termini exclude non-specific association of Tma17p with FAS. Henceforth, we will refer to Tma17p as the FAS γ subunit, to FAS devoid of the γ subunit as Δγ-FAS.

The FAS γ Subunit Regulates the Activity in Response to the Abundance of Its Co-substrate NADPH

To gather insights into the function of the γ subunit, we analyzed FAS steady-state kinetics both in its presence and absence and measured the rates of FAS substrate turnover with respect to varying concentrations of the substrates acetyl-CoA, malonyl-CoA, and NADPH. This analysis revealed substrate-excess

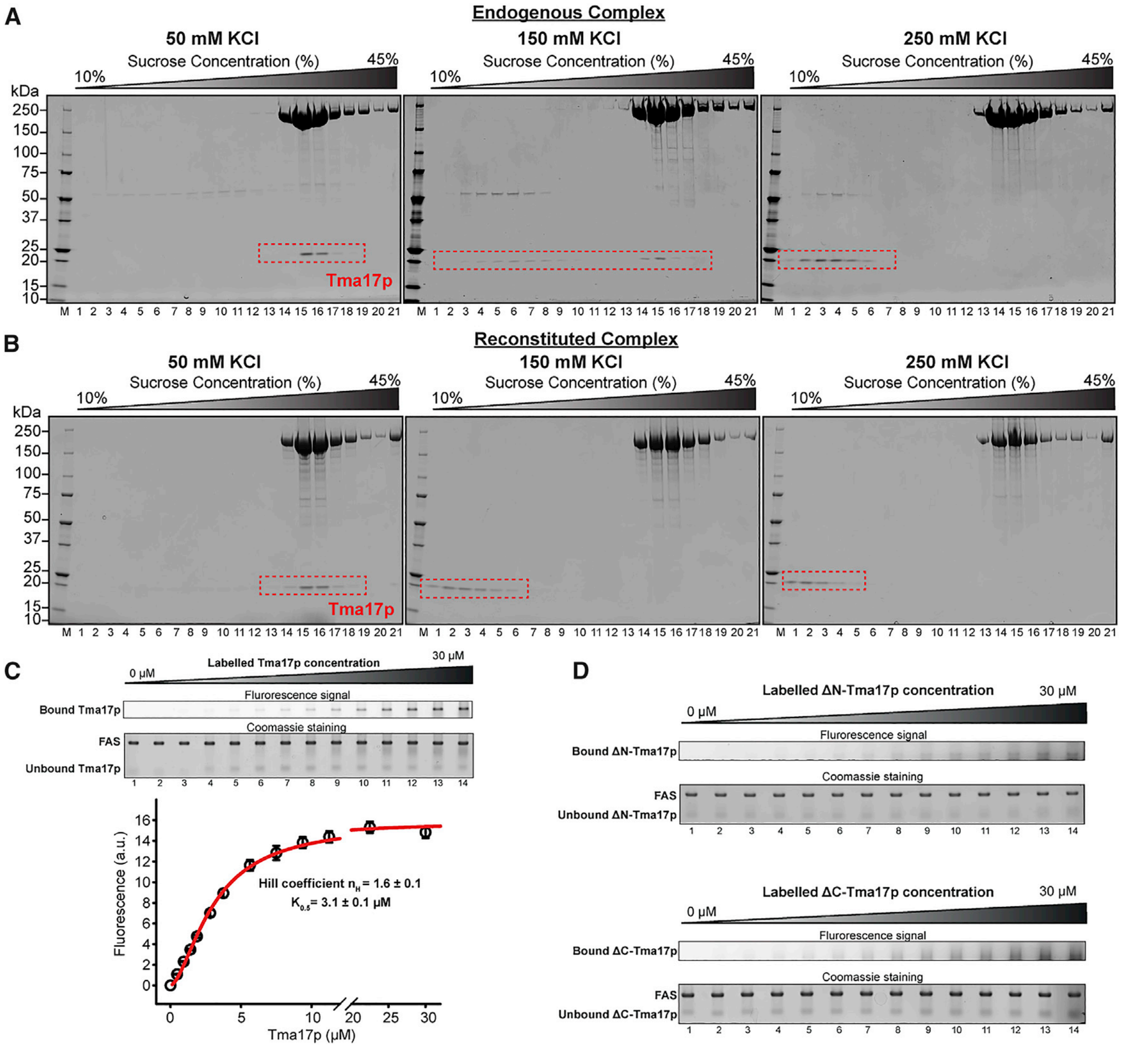

Figure 2. Tma17p Constitutes a Bona Fide γ Subunit of Yeast FAS

(A) Tma17p is bound to FAS in a salt-labile manner. SDS-PAGE analysis of sucrose density gradient centrifugation of wild-type *S. cerevisiae* FAS at different ionic strength conditions. At 50 mM KCl (left panel), Tma17p binds FAS and co-sediments in the 40S region of the gradient (lanes 14–17). At 150 mM KCl (middle panel), Tma17p is partially dissociated (lanes 2–9 and 14–17), while at 250 mM KCl (right panel), Tma17p is completely dissociated from FAS and sediments in the top fractions of the gradient akin to free Tma17p (lanes 1–7).

(B) SDS-PAGE analysis of sucrose density gradient centrifugation of reconstituted FAS/rTma17p complex at different ionic strength conditions. Recombinant Tma17p is stably associated with FAS at 50 mM KCl but completely dissociates at 150 mM KCl (lanes 1–6 and 14–17).

(C) Reconstitution of the FAS/Tma17p complex. The top panel depicts a Coomassie-stained native gel, where the positions of ΔTma17p-FAS and Tma17p are indicated. The middle panel shows the fluorescence of the FAS region to visualize FAS-bound Tma17p. The lower panel represents the quantitative analysis of the fluorescence signal using the Hill equation (Equation 1 in the STAR Methods). Error bars represent SD.

(D) Reconstitution of the FAS/Tma17p complex using recombinant Tma17p with either an N-terminal (1–24) or C-terminal (117–150) deletion. Compared to rTma17p shown in (C), the removal of N- or C-terminal segments leads to poor or no binding to FAS.

inhibition for both acetyl-CoA and malonyl-CoA, and a moderate modulation of the maximum rate (V_{max}), substrate affinity ($K_{0.5}^{app}$), cooperativity of substrate binding (Hill coefficient n_H), and substrate inhibition (K_i) by the γ subunit (Figures 3A and 3B). In contrast, the analysis of steady-state kinetics at different NADPH concentrations revealed a direct impact of the γ subunit on NADPH binding and processing by FAS (Figures 3C–3F). With Δγ-FAS, steady-state conditions are established at once such that the measured initial and steady-state rates are equal. In contrast, FAS substrate turnover progress curves exhibit a pronounced hysteretic behavior in the presence of the γ subunit. FAS displays a smaller activity ($v_0 > 0$) and undergoes a mono-exponential activation phase to establish steady state with a multi-fold enhanced activity ($v_{ss} > v_0$) before substrate depletion sets in (Figures 3C, 3D, and S2). The apparent Michaelis constant ($K_{0.5}^{app}$) for NADPH is lower in the case of Δγ-FAS and increased 3-fold in the presence of the γ subunit both for initial and steady-state rates (Figure 3E). This effect elicited

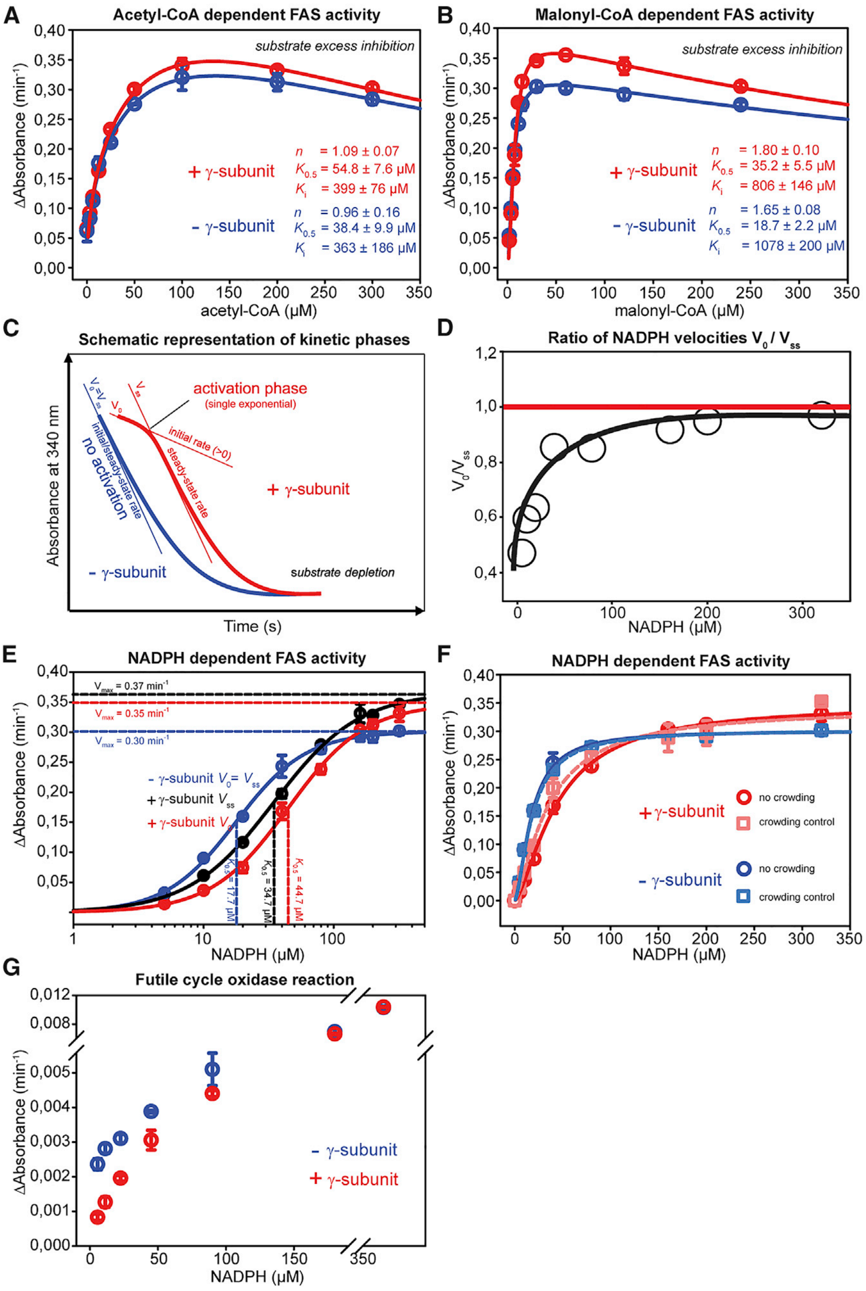

Figure 3. Steady-State Kinetic Analysis of FAS in Absence and Presence of γ Subunit

(A) FAS activity at different acetyl-CoA concentrations in presence (red) and absence (blue) of the γ subunit. In both cases, no apparent cooperativity (*n* ~1) but a pronounced substrate excess inhibition (>100 µM acetyl-CoA) was detected. Error bars represent SD.

(B) FAS activity at different malonyl-CoA concentrations in presence (red) and absence (blue) of the γ subunit. Under both conditions, a positive cooperativity and a substrate excess inhibition (>50 µM malonyl) were detected. Error bars represent SD.

(C) Schematic representation of the progress curves of FAS-catalyzed substrate turnover obtained at low NADPH concentrations. Without the γ subunit (blue), the steady state is immediately established upon mixing (initial rate v_0 = steady-state rate v_{ss}). In the presence of the γ subunit (red), FAS is subject to activation, where a mono-exponential phase transition occurs from a small initial activity v_0 to an enhanced steady-state activity v_{ss}.

(D) Plot showing the ratio of v_0/v_{ss} FAS-activity at increasing NADPH concentrations.

(E) Substrate dependence for co-substrate NADPH in absence (blue) and presence (red) of the γ subunit considering initial and steady-state rates. Note the enhanced activity of FAS in presence of the γ subunit at saturating NADPH concentrations and the altered apparent substrate dissociation constants $K_{0.5}$ (see main text). Error bars represent SD.

(F) FAS activity at different NADPH concentrations in presence (red) or absence (blue) of the γ subunit under crowding (light red/light blue, dashed lines) versus non-crowding conditions. All measurements reveal a positive cooperativity. Addition of the γ subunit leads to a shift of the $K_{0.5}$ and increasing V_{max}. Measurements under crowding conditions indicate the specificity of the γ subunit. Error bars represent SD

(G) FAS futile cycle activity in the presence of NADPH only (acetyl- and malonyl-CoA omitted). At lower NADPH-concentrations, transfer of the reducing equivalents from NADPH to oxygen via the FMN cofactor is suppressed in presence of the γ subunit (red) compared to in its absence (blue). Error bars represent SD.

by the γ subunit is more pronounced at low NADPH concentrations and almost absent at higher concentrations, where the initial rate nearly equals the steady-state rate (Figures 3C, 3D, and S2). Steady-state conditions are established after ~20 s, implying that a slow, large-scale conformational change coincides with activation. Even the addition of high molar excesses of trypsin inhibitor as a control (Figure 3F) exerted no such effect, highlighting γ subunit specificity. At high NADPH concentrations (≥100 µM), the γ subunit enhances the activity of FAS in comparison to Δγ-FAS by ~25%, whereas at lower NADPH concentrations, it slows the turnover rate of FAS almost 2-fold.

We also observed NADPH to be consumed by FAS in the ER domain even in the absence of acetyl-CoA and malonyl-CoA (Figure 3G), where a possible deleterious side reaction can occur: the NADPH-dependent oxidation of oxygen by the FMN cofactor to form reactive oxygen species including H_2O_2 (Chaiyen et al., 2012). We recognized that the γ subunit retards NADPH turnover in the absence of the substrates acetyl- and malonyl-CoA (Figure 3G). Therefore, the γ subunit additionally enhances the productivity of FAS by suppressing ER domain futile cycles.

Together, the kinetic data show that the γ subunit impacts FAS enzymatic activity, in particular the reductase activities, such that the NADPH-dependence dynamic range is broadened to

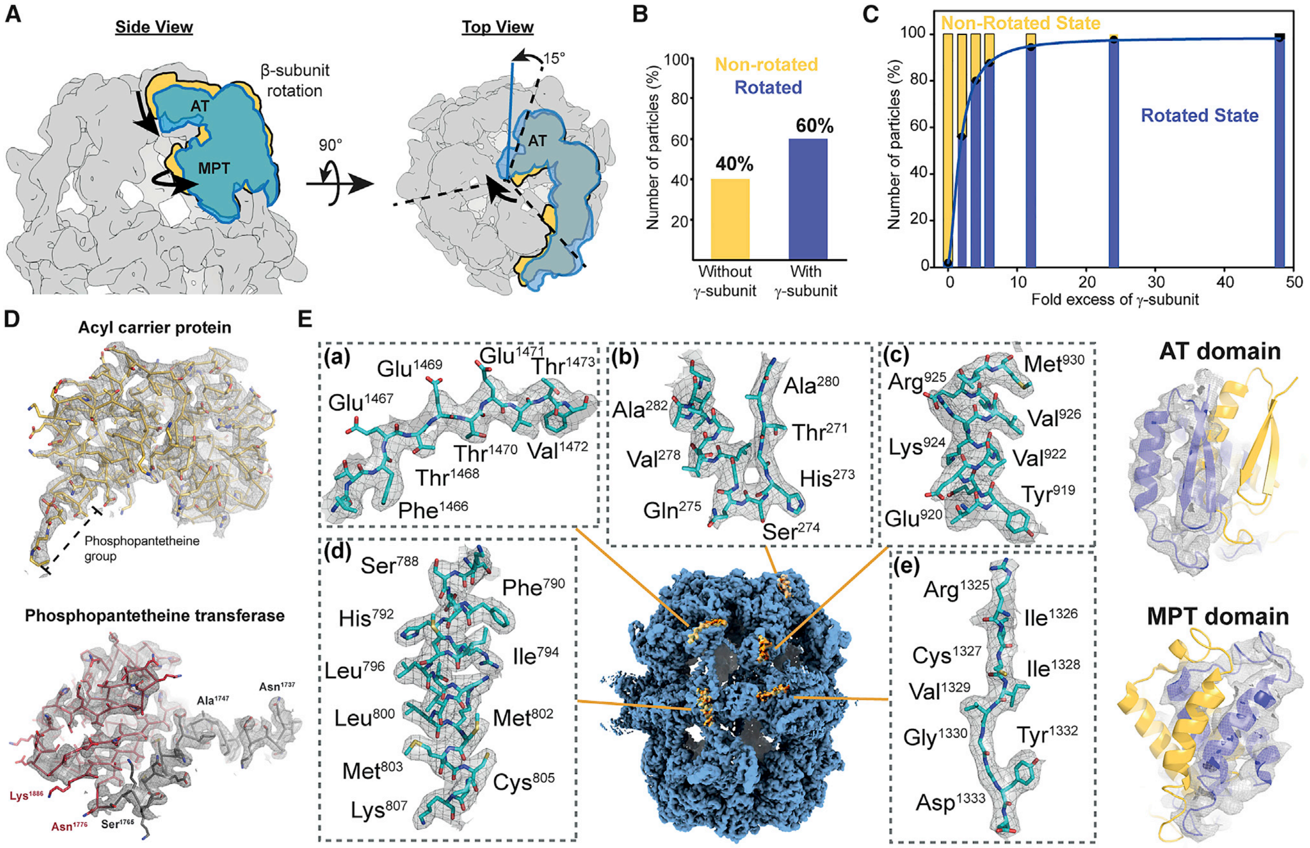

Figure 4. High-Resolution Structure Determination of Yeast FAS in Two Major Conformations

(A) Overlay of β-subunits of the non-rotated (yellow) and rotated (blue) conformations obtained in initial cryo-EM structure determination stages. The rotated conformation is attained by a swivel of each β-subunit by 15° with respect to the 3-fold symmetry axis and a compaction of the overall dimensions of FAS by 10 Å. This results in an inward shift of the AT domains and an outward movement of the MPT domains. The central 3-fold axis of the FAS molecule is indicated as dashed lines in the top view.

(B) The ratio of FAS particle abundance adopting either non-rotated or rotated conformations of the endogenous FAS/γ subunit complex is depicted.

(C) Analysis of particle abundance in the non-rotated or rotated conformation in response to increasing amounts of the γ subunit.

(D) The ACP (top) and PPT (bottom) domain models with their corresponding $2mF_o$-DF_c density from the Δγ-FAS crystal structure are shown. In contrast to previous structures, the whole phosphopantetheine prosthetic group attached to Ser^{180} is traceable in the density maps. The C-terminal segment of the α-subunit comprising an α-helix (Ala^{1747}-Ser^{1765}) and the PPT domain (Asn^{1776}-Lys^{1886}) were also elusive in earlier structures.

(E) Cryo-EM structure of the FAS/γ subunit complex calculated with imposed D3 symmetry at 2.8 Å resolution. Several sections within (a) DH, (b) AT, (c) ER, (d) KR, and (e) KS domains (cyan) are displayed with their corresponding density (left panel). The shift in the AT and MPT domain-upon-domain rotation is shown, overlaid with the densities corresponding to the rotated conformation as a mesh (right panel).

accommodate differences in cellular metabolism. The estimated $K_{0.5}^{app}$ of Δγ-FAS for NADPH (17.7 μM) is significantly lower than reported cellular concentrations of NADPH (50–150 μM) (Gancedo and Gancedo, 1973; Polakis and Bartley, 1966), implying that FAS activity, if left unregulated, would rapidly deplete NADPH, jeopardizing cellular survival. The γ subunit allows cells to regulate FAS activity over an enhanced concentration regime of NADPH, well within the physiological range.

The γ Subunit Stabilizes a Rotated FAS Conformation

Having established that Tma17p constitutes an authentic, regulatory γ subunit of FAS, we asked whether its binding impacts the overall structure of FAS. We set out to solve the structure of FAS co-purified with the γ subunit by cryoelectron microscopy (cryo-EM). We recognized that two predominant FAS conformations are imaged, either with a non-rotated or with a rotated dome structure (Figure 4A). Both conformations are related to each other by an ~15° twist with respect to the central 3-fold symmetry axis at the top of the dome. This results in an inward shift of the AT domain and an outward shift of the MPT domain. 40% single particles adopted the non-rotated conformation, while 60% single particles resided in the rotated one (Figure 4B). Could the existence of one or both of these conformations correlate with the γ subunit? Considering the relatively weak affinity of the γ subunit to FAS, and the fact that cryo-EM grids were prepared at a concentration of 0.2 μM FAS, we surmised that partial γ subunit dissociation might have occurred, eliciting conformational heterogeneity. By reconstituting Δγ-FAS with increasing amounts of the γ subunit and counting particles in either the non-rotated or rotated conformation on cryo-EM grids

(Figure 4C), we found that the abundance of particles in the rotated state correlates with the amount of γ subunit added.

With this information, we proceeded to determine high-resolution structures of FAS in both conformations. For the non-rotated conformation, we initially grew crystals of Δγ-FAS, which belong to the primitive monoclinic space group $P2_1$ with unit cell constants of a = 217.6 Å, b = 347.6 Å, c = 265.3 Å, and β = 107.9° and contain a single Δγ-FAS in the asymmetric unit and diffracted X-rays to 2.9 Å (Table S2). The structure revealed excellent electron density throughout the molecule (Figures 4D and S3A; Table S2). Analysis of the diffraction data with the STARANISO server indicated mild anisotropy of 0.1–0.2 Å along the various unit cell directions. Anisotropic truncation of the data improved refinement of the model, resulting in lower average B-factors and R_{work}/R_{free} of 19.2%/21.1% (Figures S3B–S3D; Table S2). This crystal structure in the non-rotated conformation, where all functional domains of FAS are clearly resolved, is the basis for all models of FAS described in this article. This is exemplified by the ability to clearly resolve the phosphopantetheine prosthetic group attached to Ser180 of the ACP domain, as well as the entire PPT domain (Figure 4D). We were also able to obtain a Δγ-FAS structure in the non-rotated conformation by cryo-EM at global resolutions, estimated using the 0.143 Fourier shell correlation (FSC) criterion of 2.9 Å with applied D3 symmetry, 3.0 Å with applied C3 symmetry, and 3.3 Å in asymmetric reconstructions (Figure S4; Table S2). This cryo-EM dataset contained 92% single particles in the non-rotated state and 8% in the rotated conformation, suggesting that there is a dynamic equilibrium between non-rotated and rotated conformations and the latter is stabilized by the γ subunit.

We then proceeded to determine the structure of the reconstituted FAS/γ subunit complex. This dataset was essentially devoid of particles in the non-rotated conformation, corroborating that the γ subunit stabilizes the rotated FAS conformation. We were able to reconstruct a cryo-EM structure in the rotated conformation at a global resolution, estimated using the 0.143 FSC criterion of 2.8 Å with applied D3 symmetry, 2.9 Å with applied C3 symmetry, and 3.2 Å in asymmetric reconstructions (Figure S5; Table S2). The quality of the cryo-EM map allowed the reliable modeling of the rotated FAS conformation (Figure 4E). To ensure that the rotated conformation was not spuriously stabilized by the dissociation of the γ subunit at the protein concentrations employed for cryo-EM grid preparation, we also grew crystals of the reconstituted FAS/γ subunit complex at higher protein concentrations. We obtained crystals of the FAS/γ subunit complex, which belong to the primitive monoclinic space group $P2_1$ with unit cell constants of a = 234.9Å, b = 430.3Å, c = 422.6Å, and β = 97°, that contain two FAS molecules in the asymmetric unit and diffracted X-rays to 4.6 Å resolution (Table S2). The FAS/γ subunit crystal structure was solved by molecular replacement using the Δγ-FAS crystal structure described above, which allowed for the reliable modeling of a Cα-trace and confirmed that the rotated conformation is indeed attained in the presence of the γ subunit (Figure S6). The similarity among models derived from cryo-EM and X-ray crystallography for both dome conformations enables a conclusive interpretation of the structural impact of γ subunit binding (Table S2). Notably, these findings are not flawed by different crystal contacts or imposed symmetry in calculation of the cryo-EM structures and allow for cross-validation of the structural data. In summary, the high-resolution structures of FAS in non-rotated and rotated conformations suggest that the two states are linked in a spontaneous thermodynamically controlled manner, and binding of the γ subunit to the FAS stabilizes the rotated conformation.

Rearrangement of the Dynamic ACP Domain in the Rotated FAS Dome and Architecture of the γ Subunit

The large-scale rearrangements to attain the rotated conformation of the FAS dome (Figure 4A) appear to be predominantly driven by rigid-body motions rather than conformational changes within the enzymatic domains (Table S2). Structures of both conformations at high-resolution allow us to address the questions: (1) do conformational changes in the FAS dome impact the ACP domain, and (2) does the γ subunit architecture when bound to FAS, explain how it modulates FAS activity.

In the non-rotated Δγ-FAS structure, all ACP domains are found in close proximity to the KS site (Figure 5A, left panel), as previously reported (Johansson et al., 2008; Leibundgut et al., 2007; Lomakin et al., 2007). In contrast, all ACP domains are found in proximity to the AT domain in the rotated, γ subunit bound FAS structure (Figures 5A and S6). This ACP domain position is unambiguously evidenced by positive difference density- and omit-maps of the rotated FAS crystal structure (Figure S6), as well as in the cryo-EM density (Figure 5A). Thus, the γ subunit stabilized rotated dome structure appears to coincide with ACP domain relocation to AT domains. This rotated to non-rotated conformational transition of the dome most likely is the basis for the hysteretic behavior of FAS (Figures 3C–3F and S2). Is the rotated conformation a consequence of the γ subunit directly stabilizing this ACP domain position? Favoring this hypothesis, we found 12 additional cryo-EM density elements within rotated FAS domes (Figure 5B) that were cross-validated in difference density- and omit-maps of the rotated FAS crystal structure (Figure S6), and cannot be explained by FAS α- or β-subunits. The densities displayed sufficient detail that allowed for modeling the γ subunit sequence in a visible coiled-coil segment (Figures 5C and S6). The density element juxtaposed to the ER domain could be modeled by the N-terminal portion of the γ subunit, whereas its C-terminal 18 residues could be modeled into density contacting the KR active site (Figure 5C). This structural model of the γ subunit was independently validated by crosslinking mass spectrometry (XL-MS) (Figures 5D and S7) using three cross-linkers: BS3, SDA, and EDC-NHS (with spacer arms lengths of 11.4 Å, 3.9 Å, and 0 Å, respectively). In addition, XL-MS revealed a spatial proximity of the central part of the γ subunit (residues 60–75) to the MPT domain and an association of residues 110–130 of the γ subunit with the KR domain. These segments of the γ subunit are flexible and poorly resolved in the cryo-EM density. Moreover, the cryo-EM γ subunit model fits the difference density of the rotated FAS crystal structure and strongly resembles *ab initio* models generated by Robetta (Kim et al., 2004) (data not shown).

Closer inspection of the FAS-bound γ subunit architecture revealed that the N-terminal part occludes the ER active site, whereas the C-terminal 18 residues of the γ subunit occupy the KR domain active site (Figure 5E). This (1) rationalizes why NADPH binding and processing is modulated by the γ subunit

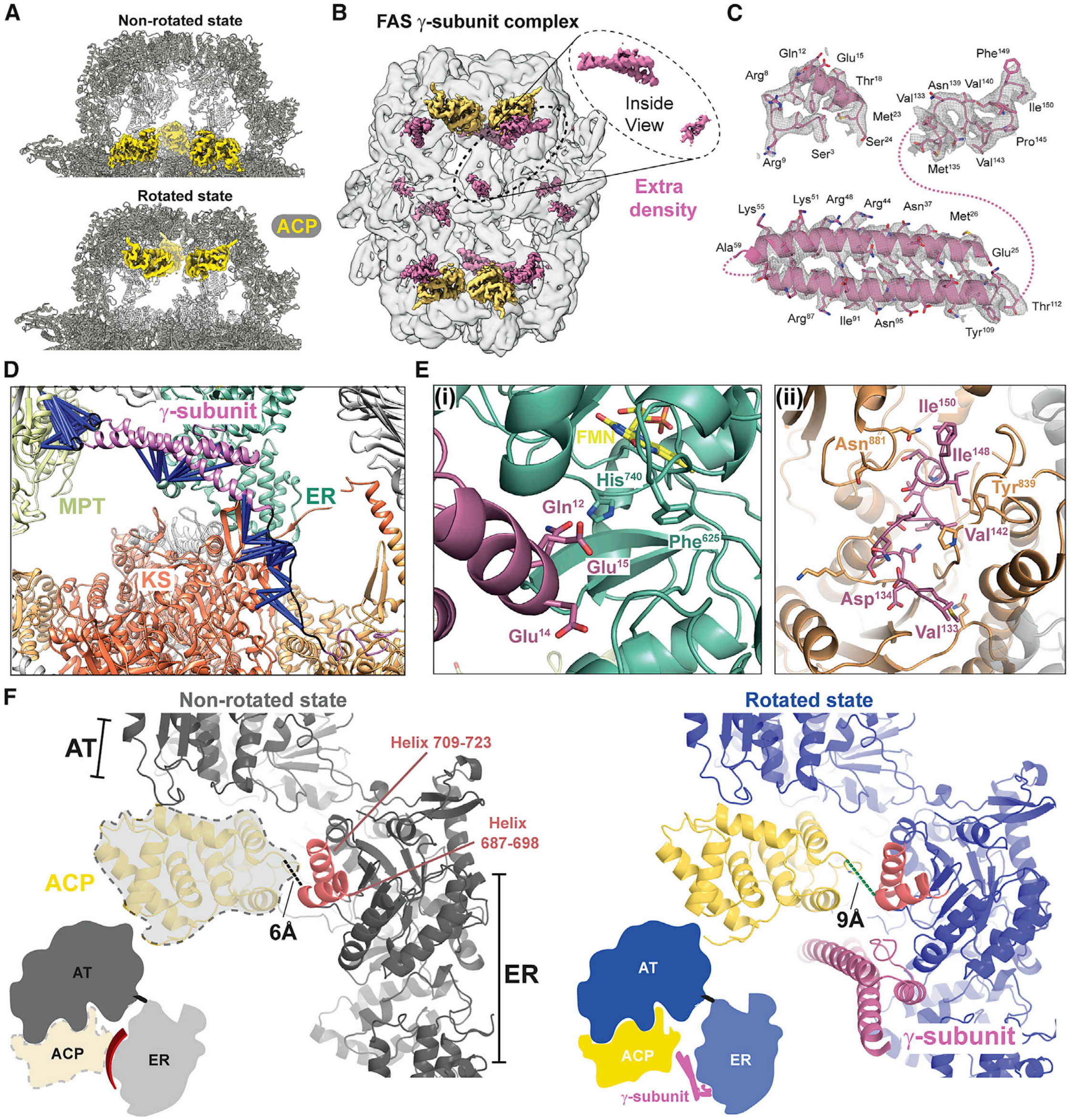

Figure 5. Structural Differences Elicited in FAS upon Binding of the γ Subunit

(A) Rotation of the β-subunit correlates with altered ACP positions. In the top panel, the non-rotated conformation is shown, where ACP domains (yellow) are found adjacent to the KS. In the rotated conformation depicted in the bottom panel, the ACP domains are found in proximity to the AT.

(B) In the FAS/γ subunit complex, an additional coiled-coil density is detected adjacent to ACP domains, as well as a small density fragment at the KR domains. These extra densities were found to correspond to the bound γ subunit.

(C) The structural model of the γ subunit is shown. Cryo-EM density for most of the side chains can be visualized. No density for residues 60–76 and 114–132 is found, most likely owing to structural flexibility of these segments.

(D) Xl-MS was used to validate the γ subunit structural model. The composite of crosslinks obtained using BS3, SDA, and EDC-NHS is mapped onto the FAS/γ subunit complex structure. The N-terminal region of the γ subunit is positioned at the ER domain, a central part in proximity to the MPT domain, whereas the C-terminal part appears to contact the KR and KS domains.

(E) The N-terminal part of the γ subunit occludes the ER active site, where acidic residues (Glu14, Glu15) protrude into the NADPH binding cleft (i). The 18 C-terminal residues of the γ subunit occupy the NADPH binding cleft in the KR active site (ii).

(F) In the non-rotated state, the ER and AT domain distance is shorter in comparison to the rotated state. An attempt to dock the ACP in the AT domain position with FAS dome in the non-rotated conformation (left), suggests that two ER-domain helices (salmon) constrict the space for ACP binding to the AT domain. The rotated FAS conformation enables spatial accommodation of the ACP at the AT domain and the γ subunit coiled-coil acts as a wedge in between AT and ER domains to stabilize the rotated conformation.

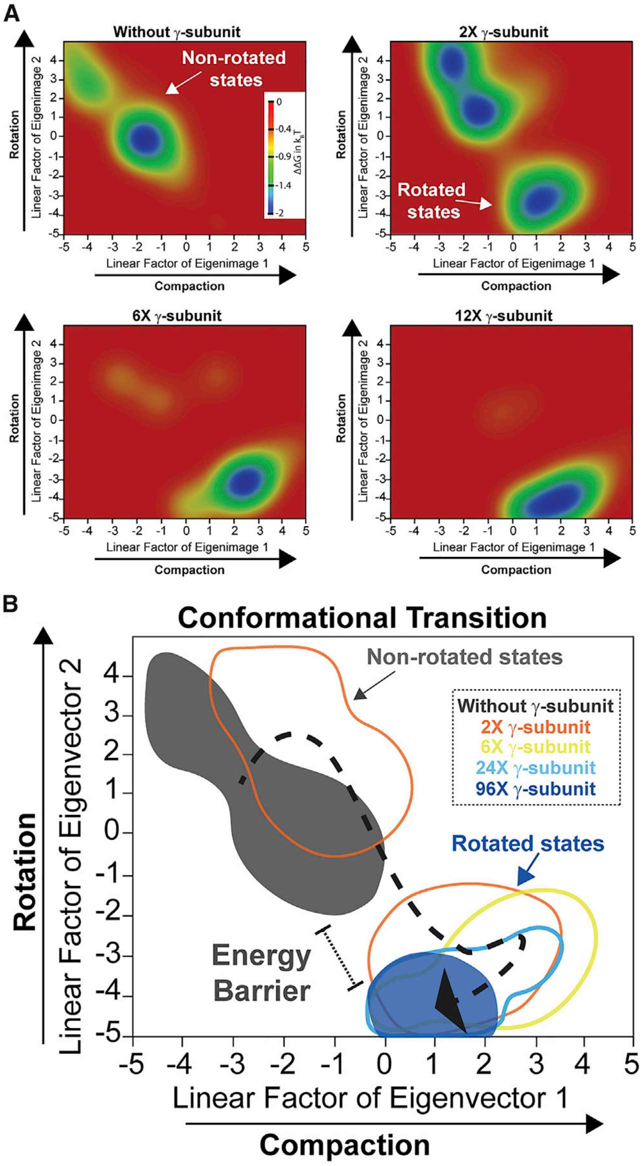

Figure 6. Energy Landscape Analysis of FAS Conformations Induced by the γ Subunit

(A) The x axis of all plots corresponds to the linear factor of the first eigenimage, which describes FAS compaction. The y axis corresponds to the linear factor of the second eigenimage, which describes FAS dome rotation. The $\Delta\gamma$-FAS adopts a non-rotated conformation (top left), addition of a 2-fold molar excess of the γ subunit (top right), leads to the population of both rotated and non-rotated conformations. Further increase in γ subunit concentration to a 6- (bottom left) and 12-fold (bottom right) molar excess results exclusively in rotated FAS.

(B) Overlay of the energy landscape plots of the FAS in the presence of increasing concentrations of the γ subunit. The energy landscapes indicate that γ subunit binding results in the formation of an energy barrier at 4°C to attain the non-rotated conformation, with a smooth transition and some additional conformational intermediates. The dotted black line indicates the transition path to the rotated FAS conformation.

(Figures 3E and 3F), (2) provides a structural basis for the observed hysteretic behavior (Figures 3C–3F and S2), and (3) addresses how the formation of off-pathway reactive oxygen species is suppressed at the ER domain (Figure 3G). ACP binding to the AT domain upon dome rotation is not restrained in the rotated conformation, where it is additionally stabilized by γ subunit interactions with the ER and MPT domains and additional electrostatic γ subunit/ACP interaction (Figure S6). Whereas in the non-rotated state, two helices of the ER domain—encompassing β-subunit residues 687–698 and 709–723, respectively—constrict the space required for the ACP to bind the AT domain (Figure 5F). Rearrangement of these helices, both in the presence and absence of the γ subunit, facilitates ACP binding to the AT domain. Together, the γ subunit spans a distance of $\sim$120 Å inside the cavity of the FAS dome, structurally modulates access of NADPH to the processing reductase domains, and drives a wedge (the coiled-coil segment) into the AT-ER interface to stabilize the rotated conformation and ACP domain binding to AT domains.

Conformational and Energetic Impact of γ Subunit Binding

The structural findings described in Figures 4 and 5 indicate that γ subunit binding impacts the FAS conformational landscape. Non-rotated and rotated states appear to co-exist in a thermodynamic, interchanging equilibrium with the γ subunit stabilizing the rotated conformation, which is the basis of the observed kinetic hysteresis (Figure 3). To further characterize and interrogate the thermodynamics of these functionally important γ subunit-induced conformational changes, we applied our method of 3D classification combined with energy landscape calculation (Haselbach et al., 2017, 2018). We collected individual cryo-EM datasets of $\Delta\gamma$-FAS, reconstituted with increasing concentrations of the γ subunit, and refined 3D structures of each individual dataset with a mask corresponding to the central wheel. To assess the conformational space occupied by the dome in each individual dataset, we then performed a 3D-classification without alignment in batches of 6,500 particles each, relying exclusively on the previously obtained alignment parameters of the central wheel. The individual 3D classes were refined to ensure their validity and subsequently subjected to 3D principal component analysis (PCA). The first eigenvector of this 3D PCA describes the compaction of the dome, whereas the second eigenvector signifies the notable rotation of the dome (Video S1). The number of particles in each 3D class was then used to map an energy landscape by performing a Boltzmann interpolation in a coordinate system that is defined by the first and second eigenvectors of the PCA. The energy landscapes, shown in Figure 6, for each individual dataset recapitulate the observation that binding of the γ subunit and ensuing formation of the FAS/γ subunit complex results in the adoption of the rotated conformation. Moreover, the energy landscapes indicate that γ subunit binding generates an energy barrier at 4°C (where the experiments were performed), restricting kinetic access to the non-rotated conformation. The energy difference between the two FAS conformations was found to be in the range of $\sim$2 k_BT, which suggests that thermal energy is sufficient to drive conformational changes in FAS. The stabilization of the rotated conformation by the energy barrier formed by the γ subunit most likely serves to open a kinetic window for the regulation of the enzymatic activity of FAS.

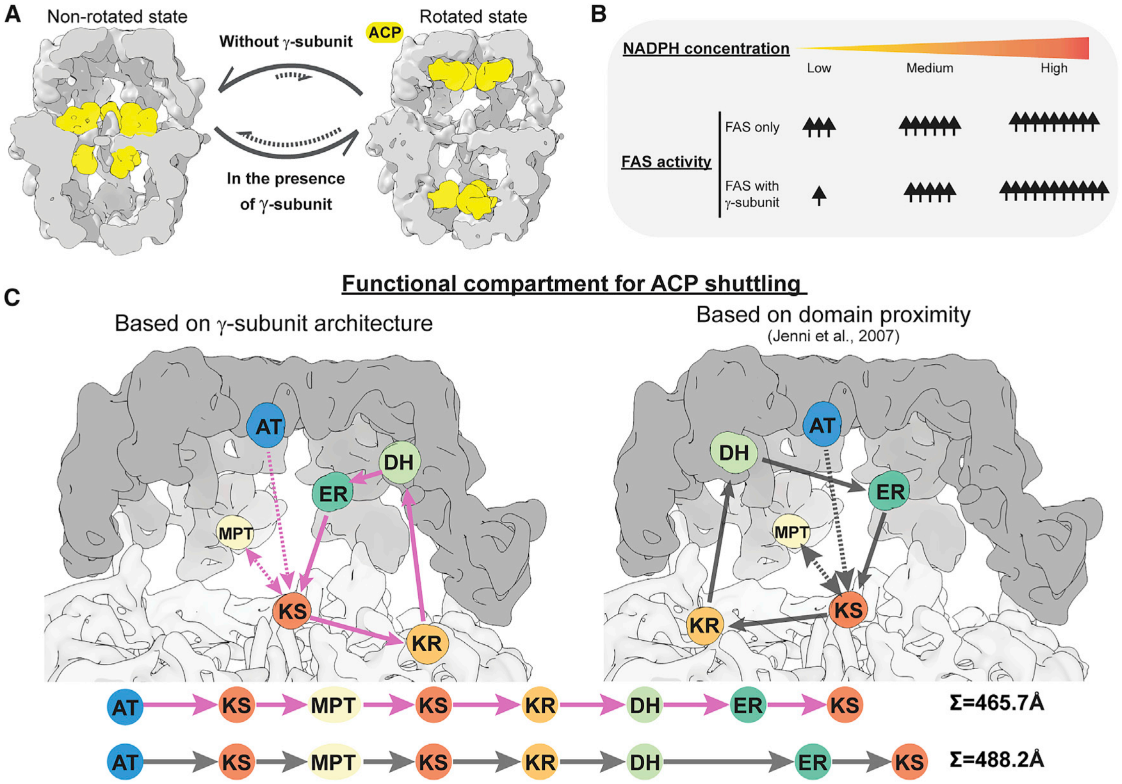

Figure 7. The Regulatory γ Subunit Impacts FAS Conformation Equilibria and Directly Regulates FAS Activity

(A) The transition from a non-rotated to a rotated FAS is coupled to the internal ACP movement from the central wheel toward the top of the dome. In the FAS/γ subunit complex, the γ subunit shifts the equilibrium to additionally stabilize the rotated state.

(B) Binding of the γ subunit allows tailoring FAS activity in response to changes in the metabolic state of the cell. In the absence of the γ subunit, FAS activity would remain high irrespective of cellular NADPH concentrations. The γ subunit is a decelerator at small, limiting NADPH concentrations, but an accelerator at non-limiting conditions. Thus, the γ subunit directly regulates FAS activity.

(C) Total distances of ACP movement within the FAS dome in the initial fatty acid synthetic cycle. ACP shuttling within the functional unit defined by γ subunit binding (left) would offer an advantage due to a shorter DH-ER distance in comparison to ACP shuttling models proposed earlier (right). The total distance traveled for one cycle in both models is shown at the bottom.

DISCUSSION

In this article, we report the discovery of a weakly associated, regulatory γ subunit of the yeast FAS, which has escaped detection in over 50 years of research on this essential multi-enzyme complex. We have applied a series of biochemical and enzymological approaches and further determined high-resolution structures, by both X-ray crystallography and single particle cryo-EM, to elucidate the function of the regulatory γ subunit within the context of FAS. The γ subunit, a 17-kDa protein, co-sediments with FAS in the 40S region and reproducibly co-purifies. Further, six molecules of the γ subunit can bind per FAS molecule in a cooperative manner with an affinity in the low μM range. At this time, however, whether *in vivo* FAS is always saturated by six molecules of the γ subunit, or FAS species exist, where sub-saturating amounts of γ subunit are bound, remains to be seen.

Functionally, the γ subunit modulates NADPH binding and processing indicated by kinetic hysteresis (Figures 3C–3F). At low NADPH concentrations, the initial rate of substrate turnover by FAS is reduced by the γ subunit by a factor of two. A slow exponential activation phase follows to establish true steady-state turnover conditions, which most likely depend on large-scale conformational rearrangements. At high NADPH concentrations, the γ subunit increases substrate turnover by 25% (Figures 3D–F), simultaneously, it suppresses futile cycling of NADPH at the ER domain caused by the NADPH-dependent formation of off-pathway reactive oxygen species (Figure 3G). This is achieved by the γ subunit N-terminal 24 residues occluding and kinetically retarding NADPH binding and reduction by the FMN cofactor at the ER domain active site (Figure 5E, panel i). Considering the $K_{0.5}^{app}$ of Δγ-FAS, which lies well below reported cellular concentration ranges of NADPH (Gancedo and Gancedo, 1973; Polakis and Bartley, 1966), the control exerted by the γ subunit serves to keep a potential over-consumption of NADPH by FAS in check (Figure 7B). While the γ subunit-induced modulation of NADPH binding and processing by kinetic hysteresis is most apparent (Figures 3C–3F and S2), we note that the γ subunit also exerts changes in the $K_{0.5}^{app}$ of both acetyl- and malonyl-CoA (Figure 3A and 3B), which may also minimize the risk of FAS depleting cellular pools of these two co-substrates (Shpilka et al., 2015).

Structurally, Δγ-FAS was found to mainly adopt a non-rotated conformation, where the ACP domain is located at the KS domain (Figure 7A). However, in the presence of the γ subunit, the FAS predominantly adopts the rotated conformation, where the FAS β-subunits swivel around the 3-fold symmetry axis, and the ACP domains are localized to the AT domain. The γ subunit thus directly regulates FAS activity by forming a complex and modulating its conformational landscape.

A Weakly, yet Specifically Associated, Regulatory γ Subunit of Yeast FAS

In this study, we adapted a non-chromatographic strategy to the yeast FAS, which allows for the high-yield purification of large macromolecular assemblies at a constant ionic strength and pH (Haselbach et al., 2017; Schrader et al., 2016). FAS purified by this method was quantitatively saturated by the γ subunit (Figure 1E). This protein has been shown to be associated with the translational machinery (Fleischer et al., 2006), to act as an assembly chaperone for the regulatory particle of the proteasome during stress (Hanssum et al., 2014), and in our own experiments, to be a regulator of FAS activity. How are these seemingly unrelated functions exerted by the same protein? The association of the γ subunit with the translation machinery seems to be a mischaracterization. In their original paper, Fleischer et al. (2006) clearly show that FAS co-sediments with the γ subunit, and the purification of TAP-tagged γ subunit most strongly enriches FAS α- and β-subunits but is devoid of any translational machinery component. The proposed function as an assembly chaperone for the proteasome regulatory particle (Hanssum et al., 2014) is fully contradictory to the sedimentation of this protein in the 40S range and is further questioned by the lack of a direct demonstration of biochemical interaction in yeast cells or extracts. However, we note that stimulation of γ subunit and proteasome assembly machinery expression levels genetically interact (Costanzo et al., 2010) and are controlled by similar signaling pathways (Rousseau and Bertolotti, 2016).

In contrast to the incongruent functions attributed to this protein by earlier studies, our results have revealed that the γ subunit is a bona fide regulator of FAS, based on the following evidence: (1) the sedimentation of the γ subunit in the 40S range and reproducible co-purification with FAS from cell extracts (Figures 1E and 2A); (2) the saturation of a single FAS molecule by maximally six γ subunit molecules (Figure 2C); (3) the sigmoidal association behavior and positive cooperativity of γ subunit binding to FAS (Figures 2C and S1D); (4) both N and C termini of the γ subunit are indispensable for its association with FAS (Figure 2D); (5) during purification, FAS is incubated with malonyl-CoA and NADPH to chase intermediates to products (STAR Methods), arguing that the γ subunit does not dissociate under turnover conditions (Figure 1E); (6) the modulation of NADPH turnover by the γ subunit (Figures 3D–3F) and the suppression of futile cycling of NADPH at the ER domain (Figure 3G); (7) trypsin inhibitor, a protein with a similar molecular weight and charge, is neither able to bind (Figure S1E) nor modulate FAS activity (Figure 3F); (8) six specific spatial sites corresponding to the γ subunit were resolved within the FAS dome (Figure 5B); (9) three different crosslinkers used for XL-MS validate the specific interaction of the γ subunit (Figure 5D); and (10) the γ subunit influences the conformational energy landscape of the FAS dome (Figures 4B, 4C, and 6) and the ACP domain position (Figure 5A).

The overwhelming experimental evidence gathered in this study rules out the possibility of a non-specific interaction between the $\alpha_6\beta_6$ FAS and the γ subunit. It is likely that the γ subunit has escaped detection due to the relatively high-salt conditions commonly employed to purify FAS; the immobilization on solid supports and spontaneous dissociation if FAS concentrations in the μM range are not maintained throughout purification. We infer that the application of chromatography-free purification as described herein for FAS, previously for proteasomes (Haselbach et al., 2017; Schrader et al., 2016) and the pyruvate dehydrogenase complex (Prajapati et al., 2019), which maintain high concentrations, will uncover regulatory subunits of many other large cellular macromolecular complexes.

Structural and Functional Implications of γ Subunit Binding to FAS

The structure of yeast FAS was described in the late 2000s by multiple groups (Gipson et al., 2010; Johansson et al., 2008; Leibundgut et al., 2007; Lomakin et al., 2007). Based on domain organization and proximity of all fatty acid synthetic domains, three functional compartments within the FAS dome were defined (Jenni et al., 2007). ACP domains within each compartment were suggested to shuttle growing fatty acid chains in a stochastic manner between different active sites in a clockwise circular trajectory (Figure 7C) (Jenni et al., 2007). This view was supported by MD simulations: although each ACP domain can reach all active sites within the FAS dome, they mainly remain within their functional compartment, governed by spatial proximity of active sites along with volume exclusion effects of neighboring ACP domains and their linker segments (Anselmi et al., 2010). However, this ACP shuttling mechanism assumed that the FAS dome remains static, undergoes no structural transitions, and is derived without knowledge about the γ subunit. The findings described herein suggest that existing ACP-domain-mediated substrate shuttling models need to be revisited.

The FAS dome can adopt at least two distinct conformational states. The non-rotated conformation, where the ACP domain is located at the KS active site, would functionally represent either acetyl group transfer to the KS active site or the condensation of the malonyl group with the KS-bound acetyl group. The second, rotated conformation, attained by the movement of AT away from ER domains accommodates the ACP domain at the AT active site and represents the acetyl group transfer step from AT to ACP. An immediate consequence of these two conformations corresponding to different catalytic states is to postulate that every FAS functional state is associated with a distinctive, yet unforeseen, conformation. This hypothesis awaits structural studies of stalled intermediates for validation.

One can infer γ subunit function from its binding mode to FAS, where it spans the inner cavity of the FAS dome, contacts three active sites (ER, MPT, and KR) and shuts down every catalytic step except the initial acetylation. The multiple domains contacted by the γ subunit could represent a functional unit within each FAS dome. If one considers all γ subunit contacts, every fatty acid synthetic active site is present but in a different spatial organization than previously suggested. In the functional compartment delineated by the γ subunit, a counter-clockwise movement of the ACP domain among processing active sites would be predicted (Figure 7C). Does this new functional spatial arrangement offer any advantage? In the functional compartment outlined by the γ subunit, most ACP-shuttle paths are similar, the distance between the ER-DH domains, however, is notably shortened by 25 Å. Additionally, the γ subunit occupies a volume corresponding to 33% of the FAS dome, eliciting molecular crowding, which has been reported to drive ACP-shuttling (Anselmi et al., 2010). Therefore, γ subunit binding should yield a different, yet partially more efficient functional cycle, which agrees well with the observed higher activity (Figures 3D–3F).

Biotechnological Implications

Aside from the mechanistic implications arising from the discovery of a FAS γ subunit, some clear biotechnological implications arise. First, the natural γ subunit structural scaffold can be exploited to introduce known natural and designed enzymatic modules into domes, such as desaturases, absent in wild-type FAS. The replacement of the flexible γ subunit linker segment between the C terminus of the coiled-coil and the KR-binding part appears predestined for this. Similar strategies have been pursued (Gajewski et al., 2017b, 2017a; Xu et al., 2016), but the strategy proposed here might be advantageous, because the γ subunit is engineered and might reduce adverse viability effects arising from direct FAS engineering. Second, mutation, segmentation, and affinity maturation may allow the manipulation and exploitation of the γ subunit MPT-, ER-, and KR-binding segments as isolated peptides into generalized fatty acid synthase inhibitors (Figure S7). Such compounds will be beneficial for the treatment of i.e., tuberculosis, obesity, and cancer, where FAS is already a validated target.

STAR★METHODS

Detailed methods are provided in the online version of this paper and include the following:

- KEY RESOURCES TABLE
- LEAD CONTACT AND MATERIALS AVAILABILITY
- EXPERIMENTAL MODEL AND SUBJECT DETAILS
  - Yeast culture
  - Expression of the γ subunit
- METHOD DETAILS
  - Purification of yeast FAS
  - Purification of the γ subunit
  - Salt concentration-dependent dissociation of the γ subunit
  - Binding affinity of the γ subunit to FAS
  - Steady-state kinetics
  - Preparative reconstitution of the FAS/γ subunit complex
  - Cryo-EM sample preparation
  - Cryo-EM data collection and image processing
  - Energy Landscapes
  - FAS Crystallization and Crystal Stabilization
  - X-ray Diffraction Data collection
  - X-ray structure determination
  - Cryo-EM Model building
  - Phosphorylation analysis of the γ subunit using Mass Spectrometry
  - Crosslinking Mass Spectrometry
- QUANTIFICATION AND STATISTICAL ANALYSIS
- DATA AND CODE AVAILABILITY

SUPPLEMENTAL INFORMATION

Supplemental Information can be found online at https://doi.org/10.1016/j.cell.2020.02.034.

ACKNOWLEDGMENTS

We thank Thomas Schultz for yeast fermentation, Ulf Diederichsen and Patrick Menzel for help purifying acetyl- and malonyl-CoA, Arwen Pearson for critical comments on the manuscript, and Gabi Heyne as well as Suzan van Gerwen for technical assistance. Gleb Bourenkov and Thomas Schneider are gratefully thanked for their help in X-ray data collection at the EMBL beamline P14 on the PETRA III storage ring of DESY in Hamburg, Germany. H.S. (TP A05) and H.U. (TP A10) are supported by a grant from the Deutsche Forschungsgemeinschaft (DFG SFB860). A.C. and K.T. are associated members of the DFG SFB860.

AUTHOR CONTRIBUTIONS

A.C. and H.S. conceived the work and supervised all research; K.S. and A.C. developed the purification strategy for FAS; K.S. performed the structural work with the help of A.C. and H.S.; B.G. performed enzymology with the help of K.S., V.S., K.T., and A.C.; A.L. and H.U. performed Xl-MS; A.C. wrote the manuscript with the input of K.S., B.G., K.T., and H.S. and all authors reviewed the data and the manuscript.

DECLARATION OF INTERESTS

A.C. and H.S. have filed a patent for the purification procedure described herein (EP16/17/3037, USSN 62/345,913). A.C., H.S., K.S., and B.G. have filed a patent for the exploitation of the γ subunit in a biotechnological and inhibitor development sense (EP19/16/3958).

Received: October 14, 2019
Revised: December 23, 2019
Accepted: February 12, 2020
Published: March 10, 2020; corrected online: April 2, 2020

REFERENCES

Anselmi, C., Grininger, M., Gipson, P., and Faraldo-Gómez, J.D. (2010). Mechanism of substrate shuttling by the acyl-carrier protein within the fatty acid mega-synthase. J. Am. Chem. Soc. *132*, 12357–12364.

Biermann, U., Bornscheuer, U., Meier, M.A.R., Metzger, J.O., and Schäfer, H.J. (2011). Oils and fats as renewable raw materials in chemistry. Angew. Chem. Int. Engl. *50*, 3854–3871.

Burr, G.O., and Brown, W.R. (1933). On the Fatty Acids Essential in Nutrition. Proc. Soc. Exp. Biol. Med. *30*, 1349–1352.

Chaiyen, P., Fraaije, M.W., and Mattevi, A. (2012). The enigmatic reaction of flavins with oxygen. Trends Biochem. Sci. *37*, 373–380.

Cherry, J.M., Hong, E.L., Amundsen, C., Balakrishnan, R., Binkley, G., Chan, E.T., Christie, K.R., Costanzo, M.C., Dwight, S.S., Engel, S.R., et al. (2012). Saccharomyces Genome Database: the genomics resource of budding yeast. Nucleic Acids Res. *40*, D700–D705.

Costanzo, M., Baryshnikova, A., Bellay, J., Kim, Y., Spear, E.D., Sevier, C.S., Ding, H., Koh, J.L.Y., Toufighi, K., Mostafavi, S., et al. (2010). The genetic landscape of a cell. Science *327*, 425–431.

Cox, J., and Mann, M. (2008). MaxQuant enables high peptide identification rates, individualized p.p.b.-range mass accuracies and proteome-wide protein quantification. Nat. Biotechnol. *26*, 1367–1372.

Dereeper, A., Guignon, V., Blanc, G., Audic, S., Buffet, S., Chevenet, F., Dufayard, J.-F., Guindon, S., Lefort, V., Lescot, M., et al. (2008). Phylogeny.fr: robust phylogenetic analysis for the non-specialist. Nucleic Acids Res. *36*, W465-9.

Drozdetskiy, A., Cole, C., Procter, J., and Barton, G.J. (2015). JPred4: a protein secondary structure prediction server. Nucleic Acids Res. *43* (W1), W389-94.

Emsley, P., and Cowtan, K. (2004). *Coot* : model-building tools for molecular graphics. Acta Crystallogr. D Biol. Crystallogr. *60*, 2126–2132.

Fleischer, T.C., Weaver, C.M., McAfee, K.J., Jennings, J.L., and Link, A.J. (2006). Systematic identification and functional screens of uncharacterized proteins associated with eukaryotic ribosomal complexes. Genes Dev. *20*, 1294–1307.

Gajewski, J., Pavlovic, R., Fischer, M., Boles, E., and Grininger, M. (2017a). Engineering fungal de novo fatty acid synthesis for short chain fatty acid production. Nat. Commun. *8*, 14650.

Gajewski, J., Buelens, F., Serdjukow, S., Janßen, M., Cortina, N., Grubmüller, H., and Grininger, M. (2017b). Engineering fatty acid synthases for directed polyketide production. Nat. Chem. Biol. *13*, 363–365.

Gancedo, J.M., and Gancedo, C. (1973). Concentrations of intermediary metabolites in yeast. Biochimie *55*, 205–211.

Gietz, R.D. (2014). Yeast transformation by the LiAc/SS carrier DNA/PEG method. Methods Mol. Biol. *1163*, 33–44.

Gipson, P., Mills, D.J., Wouts, R., Grininger, M., Vonck, J., and Kühlbrandt, W. (2010). Direct structural insight into the substrate-shuttling mechanism of yeast fatty acid synthase by electron cryomicroscopy. Proc. Natl. Acad. Sci. USA *107*, 9164–9169.

Goddard, T.D., Huang, C.C., Meng, E.C., Pettersen, E.F., Couch, G.S., Morris, J.H., and Ferrin, T.E. (2018). UCSF ChimeraX: Meeting modern challenges in visualization and analysis. Protein Sci. *27*, 14–25.

Graber, R., Sumida, C., and Nunez, E.A. (1994). Fatty acids and cell signal transduction. J. Lipid Mediat. Cell Signal. *9*, 91–116.

Hanssum, A., Zhong, Z., Rousseau, A., Krzyzosiak, A., Sigurdardottir, A., and Bertolotti, A. (2014). An inducible chaperone adapts proteasome assembly to stress. Mol. Cell *55*, 566–577.

Haselbach, D., Schrader, J., Lambrecht, F., Henneberg, F., Chari, A., and Stark, H. (2017). Long-range allosteric regulation of the human 26S proteasome by 20S proteasome-targeting cancer drugs. Nat. Commun. *8*, 15578.

Haselbach, D., Komarov, I., Agafonov, D.E., Hartmuth, K., Graf, B., Dybkov, O., Urlaub, H., Kastner, B., Lührmann, R., and Stark, H. (2018). Structure and Conformational Dynamics of the Human Spliceosomal B^{act} Complex. Cell *172*, 454–464.

Humphrey, S.J., Azimifar, S.B., and Mann, M. (2015). High-throughput phosphoproteomics reveals in vivo insulin signaling dynamics. Nat. Biotechnol. *33*, 990–995.

Jenni, S., Leibundgut, M., Boehringer, D., Frick, C., Mikolásek, B., and Ban, N. (2007). Structure of fungal fatty acid synthase and implications for iterative substrate shuttling. Science *316*, 254–261.

Johansson, P., Wiltschi, B., Kumari, P., Kessler, B., Vonrhein, C., Vonck, J., Oesterhelt, D., and Grininger, M. (2008). Inhibition of the fungal fatty acid synthase type I multienzyme complex. Proc. Natl. Acad. Sci. USA *105*, 12803–12808.

Kabsch, W. (2010). XDS. Acta Crystallogr. D Biol. Crystallogr. *66*, 125–132.

Kim, D.E., Chivian, D., and Baker, D. (2004). Protein structure prediction and analysis using the Robetta server. Nucleic Acids Res. *32*, W526-31.

Lebedev, A.A., Young, P., Isupov, M.N., Moroz, O.V., Vagin, A.A., and Murshudov, G.N. (2012). JLigand: a graphical tool for the CCP4 template-restraint library. Acta Crystallogr. D Biol. Crystallogr. *68*, 431–440.

Leibundgut, M., Jenni, S., Frick, C., and Ban, N. (2007). Structural basis for substrate delivery by acyl carrier protein in the yeast fatty acid synthase. Science *316*, 288–290.

Lomakin, I.B., Xiong, Y., and Steitz, T.A. (2007). The crystal structure of yeast fatty acid synthase, a cellular machine with eight active sites working together. Cell *129*, 319–332.

López, M., Lelliott, C.J., and Vidal-Puig, A. (2007). Hypothalamic fatty acid metabolism: a housekeeping pathway that regulates food intake. BioEssays *29*, 248–261.

Lust, G., and Lynen, F. (1968). The inhibition of the fatty acid synthetase multienzyme complex of yeast by long-chain acyl coenzyme A compounds. Eur. J. Biochem. *7*, 68–72.

Lynen, F. (1980). On the structure of fatty acid synthetase of yeast. Eur. J. Biochem. *112*, 431–442.

Maier, T., Leibundgut, M., and Ban, N. (2008). The crystal structure of a mammalian fatty acid synthase. Science *321*, 1315–1322.

Marella, E.R., Holkenbrink, C., Siewers, V., and Borodina, I. (2018). Engineering microbial fatty acid metabolism for biofuels and biochemicals. Curr. Opin. Biotechnol. *50*, 39–46.

Müller, C.S., Knehans, T., Davydov, D.R., Bounds, P.L., von Mandach, U., Halpert, J.R., Caflisch, A., and Koppenol, W.H. (2015). Concurrent cooperativity and substrate inhibition in the epoxidation of carbamazepine by cytochrome P450 3A4 active site mutants inspired by molecular dynamics simulations. Biochemistry *54*, 711–721.

Murshudov, G.N., Skubák, P., Lebedev, A.A., Pannu, N.S., Steiner, R.A., Nicholls, R.A., Winn, M.D., Long, F., and Vagin, A.A. (2011). REFMAC5 for the refinement of macromolecular crystal structures. Acta Crystallogr. D Biol. Crystallogr. *67*, 355–367.

Nelson, D.L., and Cox, M.M. (2012). Lehninger Principles of Biochemistry, Sixth Edition (W. H. Freeman and Company).

Notredame, C., Higgins, D.G., and Heringa, J. (2000). T-Coffee: A novel method for fast and accurate multiple sequence alignment. J. Mol. Biol. *302*, 205–217.

Pettersen, E.F., Goddard, T.D., Huang, C.C., Couch, G.S., Greenblatt, D.M., Meng, E.C., and Ferrin, T.E. (2004). UCSF Chimera–a visualization system for exploratory research and analysis. J. Comput. Chem. *25*, 1605–1612.

Polakis, E.S., and Bartley, W. (1966). Changes in the intracellular concentrations of adenosine phosphates and nicotinamide nucleotides during the aerobic growth cycle of yeast on different carbon sources. Biochem. J. *99*, 521–533.

Prajapati, S., Haselbach, D., Wittig, S., Patel, M.S., Chari, A., Schmidt, C., Stark, H., and Tittmann, K. (2019). Structural and Functional Analyses of the Human PDH Complex Suggest a “Division-of-Labor” Mechanism by Local E1 and E3 Clusters. Structure *27*, 1124–1136.

Ronnett, G.V., Kleman, A.M., Kim, E.K., Landree, L.E., and Tu, Y. (2006). Fatty acid metabolism, the central nervous system, and feeding. Obesity (Silver Spring) *14* (*Suppl 5*), 201S–207S.

Rousseau, A., and Bertolotti, A. (2016). An evolutionarily conserved pathway controls proteasome homeostasis. Nature *536*, 184–189.

Scheres, S.H.W. (2012). RELION: implementation of a Bayesian approach to cryo-EM structure determination. J. Struct. Biol. *180*, 519–530.

Schindelin, J., Arganda-Carreras, I., Frise, E., Kaynig, V., Longair, M., Pietzsch, T., Preibisch, S., Rueden, C., Saalfeld, S., Schmid, B., et al. (2012). Fiji: an open-source platform for biological-image analysis. Nat. Methods *9*, 676–682.

Schrader, J., Henneberg, F., Mata, R.A., Tittmann, K., Schneider, T.R., Stark, H., Bourenkov, G., and Chari, A. (2016). The inhibition mechanism of human 20S proteasomes enables next-generation inhibitor design. Science *353*, 594–598.

Schrödinger, L. (2015). The PyMOL Molecular Graphics System, Version 1.8 (Schrödinger, LLC).

Schweizer, E., and Hofmann, J. (2004). Microbial type I fatty acid synthases (FAS): major players in a network of cellular FAS systems. Microbiol. Mol. Biol. Rev. *68*, 501–517.

Shpilka, T., Welter, E., Borovsky, N., Amar, N., Shimron, F., Peleg, Y., and Elazar, Z. (2015). Fatty acid synthase is preferentially degraded by autophagy upon nitrogen starvation in yeast. Proc. Natl. Acad. Sci. USA *112*, 1434–1439.

Smith, S., Witkowski, A., and Joshi, A.K. (2003). Structural and functional organization of the animal fatty acid synthase. Prog. Lipid Res. *42*, 289–317.

Stoops, J.K., and Wakil, S.J. (1978). The isolation of the two subunits of yeast fatty acid synthetase. Biochem. Biophys. Res. Commun. *84*, 225–231.

Tickle, I., Flensburg, C., Keller, P., Paciorek, W., Sharff, A., Vonrhein, C., and Bricogne, G. (2018). STARANISO (Global Phasing Ltd.).

Vagin, A., and Teplyakov, A. (2010). Molecular replacement with MOLREP. Acta Crystallogr. D Biol. Crystallogr. *66*, 22–25.

Wakil, S.J., Stoops, J.K., and Joshi, V.C. (1983). Fatty acid synthesis and its regulation. Annu. Rev. Biochem. *52*, 537–579.

Wang, D., and Dubois, R.N. (2012). Associations between obesity and cancer: the role of fatty acid synthase. J. Natl. Cancer Inst. *104*, 343–345.

White, S.W., Zheng, J., Zhang, Y.-M., and Rock, C.O. (2005). The structural biology of type II fatty acid biosynthesis. Annu. Rev. Biochem. *74*, 791–831.

Wieland, F., Siess, E.A., Renner, L., Verfürth, C., and Lynen, F. (1978). Distribution of yeast fatty acid synthetase subunits: three-dimensional model of the enzyme. Proc. Natl. Acad. Sci. USA *75*, 5792–5796.

Winn, M.D., Ballard, C.C., Cowtan, K.D., Dodson, E.J., Emsley, P., Evans, P.R., Keegan, R.M., Krissinel, E.B., Leslie, A.G.W., McCoy, A., et al. (2011). Overview of the CCP4 suite and current developments. Acta Crystallogr. D Biol. Crystallogr. *67*, 235–242.

Xu, P., Qiao, K., Ahn, W.S., and Stephanopoulos, G. (2016). Engineering Yarrowia lipolytica as a platform for synthesis of drop-in transportation fuels and oleochemicals. Proc. Natl. Acad. Sci. USA *113*, 10848–10853.

Yang, B., Wu, Y.J., Zhu, M., Fan, S.B., Lin, J., Zhang, K., Li, S., Chi, H., Li, Y.X., Chen, H.F., et al. (2012). Identification of cross-linked peptides from complex samples. Nat. Methods *9*, 904–906.

Yu, A.Q., Pratomo Juwono, N.K., Leong, S.S.J., and Chang, M.W. (2014). Production of Fatty Acid-derived valuable chemicals in synthetic microbes. Front. Bioeng. Biotechnol. *2*, 78.

Zhang, K. (2016). Gctf: Real-time CTF determination and correction. J. Struct. Biol. *193*, 1–12.

Zheng, S.Q., Palovcak, E., Armache, J.P., Verba, K.A., Cheng, Y., and Agard, D.A. (2017). MotionCor2: anisotropic correction of beam-induced motion for improved cryo-electron microscopy. Nat. Methods *14*, 331–332.

Zhou, Y.J., Buijs, N.A., Siewers, V., and Nielsen, J. (2014). Fatty Acid-Derived Biofuels and Chemicals Production in Saccharomyces cerevisiae. Front. Bioeng. Biotechnol. *2*, 32.

Zivanov, J., Nakane, T., Forsberg, B.O., Kimanius, D., Hagen, W.J., Lindahl, E., and Scheres, S.H. (2018). New tools for automated high-resolution cryo-EM structure determination in RELION-3. eLife *7*, e42166.

STAR★METHODS

KEY RESOURCES TABLE

REAGENT or RESOURCE	SOURCE	IDENTIFIER
Bacterial and Virus Strains		
E. coli BL21 Star (DE3) competent cells	Thermo Scientific	Cat#C601003
Chemicals, Peptides, and Recombinant Proteins		
NHS-Rhodamine	Thermo Scientific	Cat#46406
Nicotinamide adenine dinucleotide phosphate (NADPH)	Roth	Cat#AE14.1
Bovine serum albumin	Sigma-Aldrich	Cat#A7030
Malonyl-CoA	Sigma-Aldrich	Cat#M4263
Acetyl-CoA	Sigma-Aldrich	Cat#A2181
Trypsin inhibitor	Sigma-Aldrich	Cat#T9128
Benzamidine chloride	Sigma-Aldrich	Cat#B6506
Octyl glucose neopentyl glycol (OGNG)	Anatrace	Cat#NG311
Lauryl maltose neopentyl glycol (LMNG)	Anatrace	Cat#NG310
PolyEthyleneGlycol400	Sigma-Aldrich	Cat#81172
PolyEthyleneGlycol3350	Sigma-Aldrich	Cat#88276
DTT	Roth	Cat#6908.2
TCEP	UBPbio	Cat#P1020
Bradford dye reagent	Biorad	Cat#5000205
DNase	Jena Bioscience	Cat#EN-173
Lyzozyme	Thermo Scientific	Cat#89833
BS3	Thermo Scientific	Cat#21580
EDC	Thermo Scientific	Cat#22980
NHS-Diazirine (SDA)	Thermo Scientific	Cat#26167
Sulfo-NHS	Thermo Scientific	Cat#24520
Ethylene glycol	Sigma-Aldrich	Cat#293237
Deposited Data		
Crystallographic structure of yeast fatty acid synthase	Leibundgut et al., 2007	PDB: 2UV8
Cerulenin-inhibited type I yeast Fatty Acid Synthase	Gipson et al., 2010	EMDB: 1623
Cryo-EM structure of Δγ-FAS complex	This study	PDB: 6QL6, EMDB: 4578
Cryo-EM structure of FAS/γ subunit complex	This study	PDB: 6QL5, EMDB: 4577
Crystallographic structure of Δγ-FAS complex	This study	PDB: 6QL9
Crystallographic structure of FAS/γ subunit complex	This study	PDB: 6QL7
Experimental Models: Organisms/Strains		
S. cerevisiae BJ2168 (MATa prc1-407 prb1-1122 pep4-3 leu2 trp1 ura3-52 gal2)	ATCC	ATCC208277
S. cerevisiae tma17Δ BJ2168 (MATa prc1-407 prb1-1122 pep4-3 leu2 trp1 ura3-52 gal2 tma17::kanMX)	This study	N/A
S. cerevisiae BY4714 (MATa his3Δ1 leu2Δ0 met15Δ0 ura3Δ0)	ATCC	ATCC201388
S. cerevisiae BY4714 (MATa his3Δ1 leu2Δ0 met15Δ0 ura3Δ0 tma17::kanMX)	This study	N/A
Oligonucleotides		
Δ1-25 forward 5′-GAATTGATCCCTTCACCATGATGGAACTGGCACAGATTAA-3′	Sigma-Aldrich	N/A
Δ1-25 reverse 5′-CCAGTTCCATATCGCTCATCATGGTGAAGGGATCAATT-3′	Sigma-Aldrich	N/A
Δ117-150 forward 5′-TTATCGTAAAACCGGTCATGGCAAATAAAAACATGAAGTTGAAGCCAAAGAC-3′	Sigma-Aldrich	N/A

(*Continued on next page*)

Continued

REAGENT or RESOURCE	SOURCE	IDENTIFIER
Δ117-150 reverse 5′-GTCTTTGGCTTCAACTTCA TGTTTTTATTTGCCATGACCGGTTTTACGATAA-3′	Sigma-Aldrich	N/A
TMA17_del forward 5′-TTATAAAACATAAAGCAA ATCAAAACATAATAACTACTACAAGTAACATAC GACGGATCCCCGGGTTAATTAAC-3′	Sigma-Aldrich	N/A
TMA17_del reverse 5′-ACAAAGAGTATGACGTG AAAATGATGCGCAGTAAAACTAAATCCCGTCT CGATATCATCGATGAATTCGAGCTCGTTT-3′	Sigma-Aldrich	N/A
Recombinant DNA		
Plasmid: Tma17p-His6-TEV-tag in pET151/D-TOPO® vector	This study	N/A
Plasmid: Δ1-25Tma17p-His6-TEV-tag in pET151/D-TOPO® vector	This study	N/A
Plasmid: Δ118-150Tma17p-His6-TEV-tag in pET151/D-TOPO® vector	This study	N/A
pTF267 (pFA6a-TEV-6xGly-12xHis-KanMX)	Gift from Tim Formosa	Addgene plasmid # 44093; RRID:Addgene_44093
Software and Algorithms		
CCP4	Winn et al., 2011	http://www.ccp4.ac.uk
COW suite beta	H.S. and Luettich et al., unpublished data	https://www.cow-em.de
COOT v.0.8.9	Emsley and Cowtan, 2004	https://www2.mrclmb.cam.ac.uk/personal/pemsley/coot
Gautomatch	Dr. Kai Zhang	https://www.mrc-lmb.cam.ac.uk/kzhang
Gctf	Zhang, 2016	https://www.mrc-lmb.cam.ac.uk/kzhang
FIJI/ImageJ	NIH	https://imagej.nih.gov/ij/
MOLREP	Vagin and Teplyakov, 2010	http://www.ccp4.ac.uk/html/molrep.html
JLigand	Lebedev et al., 2012	http://www.ysbl.york.ac.uk/mxstat/JLigand
Sigmaplot	Systat Software Inc.	https://systatsoftware.com/products/sigmaplot/
PyMOL	Schrödinger, 2015	https://pymol.org/2/
Refmac5	Murshudov et al., 2011	https://www2.mrc-lmb.cam.ac.uk/groups/murshudov/content/refmac/refmac.html
RELION 3.0	Zivanov et al., 2018	https://www2.mrc-lmb.cam.ac.uk/relion
Staraniso Server	Tickle et al., 2018	http://staraniso.globalphasing.org/cgibin/staraniso.cgi
UCSF Chimera	Pettersen et al., 2004	http://www.cgl.ucsf.edu/chimera
UCSF Chimera X	Goddard et al., 2018	https://www.cgl.ucsf.edu/chimerax/
XDS Program Package	Kabsch, 2010	http://xds.mpimf-heidelberg.mpg.de
pLink v.1.23	Yang et al., 2012	http://pfind.ict.ac.cn/software/pLink/
JPred4	Drozdetskiy et al., 2015	http://www.compbio.dundee.ac.uk/jpred/
T-Coffee	Notredame et al., 2000	http://tcoffee.crg.cat/

LEAD CONTACT AND MATERIALS AVAILABILITY

Further information and requests for resources and reagents should be directed to and will be fulfilled by the Lead Contact: Ashwin Chari (ashwin.chari@mpibpc.mpg.de). All unique/stable reagents generated in this study are available from the Lead Contact with a completed Materials Transfer Agreement.

EXPERIMENTAL MODEL AND SUBJECT DETAILS

Yeast culture

All yeast manipulations were performed as per standard protocols (Gietz, 2014). *Saccharomyces cerevisiae* strains BJ2168 (MATa prc1-407 prb1-1122 pep4-3 leu2 trp1 ura3-52 gal2) and tma17Δ BJ2168 (MATa prc1-407 prb1-1122 pep4-3 leu2 trp1 ura3-52 gal2 tma17::kanMX) were used in this study. tma17Δ (Δγ) BJ2168 cells were generated with the help of plasmid pTF267, pTF267 (pFA6a-TEV-6xGly-12xHis-KanMX) was a gift from Tim Formosa (Addgene plasmid # 44093; http://addgene.org/44093; RRID: Addgene_44093). Cells were grown in YPD medium in an Infors 250 l fermenter and harvested in late log phase at an OD_{600} of 9-10. Subsequently, cells were washed with cold ddH_2O and then resuspended in 2X purification buffer (0.05 M BisTris pH 6.5, 0.05 M potassium acetate, 0.01 M magnesium acetate) containing 20% (w/v) sucrose such that 2 mL of buffer was added per gram of cells. Cells were then flash frozen as beads in liquid nitrogen and stored at −80°C until further use.

Expression of the γ subunit

The γ subunit was cloned as a synthetic gene into a pET151/D-TOPO® plasmid (Geneart, Regensburg) and expressed with an N-terminal His_6-TEV-tag in BL21 Star (DE3) competent cells. The transformed cells were grown at 37°C with 180 rpm shaking until an OD_{600} of 0.5 was reached, the temperature was then decreased to 18°C and expression of the γ subunit was induced 1 h after reduction of the temperature by the addition of 0.5 mM IPTG. γ subunit was expressed for 16 h at 18°C and 180 rpm. The cells were harvested by centrifugation (5000 x g, 15 minutes, 4°C), washed with cold ddH_2O and stored at −80°C.

METHOD DETAILS

Purification of yeast FAS

The purification strategy was adapted from protocols developed earlier for the purification of human 20S and 26S proteasomes (Haselbach et al., 2017; Schrader et al., 2016). We started with 700 g of frozen cell beads (corresponding to 233 g wet cell weight of yeast), which were ground in liquid nitrogen to a fine powder using a Retsch ZM200 mill. The ground powder was thawed in a water bath at 37°C, supplemented with purification buffer (0.05 M BisTris pH 6.5, 0.05 M potassium acetate, 0.01 M magnesium acetate) to 0.33x concentration from a 10x stock, followed by the addition of sucrose powder to 20% (w/v), benzamidine chloride to 10 mM and PMSF to 1 mM (from a 100 mM stock solution in propanol). The extract was incubated at 25°C on a magnetic stirrer for 30 minutes followed by centrifugation at 30,000 x g for 30 minutes at 4°C. After centrifugation, the supernatant was filtered through 3 layers each of cheese cloth and miracloth to obtain a S30 yeast cell extract. To this, Octyl Glucose Neopentyl Glycol (OGNG) (from a 10% (w/v) stock) was added to a final concentration of 0.2% (v/v) and the extract was incubated at 30°C for 30 minutes followed by centrifugation at 100,000 x g for 1 hour at 4°C. The supernatant was again filtered through 3 layers each of cheese cloth and miracloth. The thus clarified S100 extract was subjected to differential precipitation with PolyEthyleneGlycol400 (PEG; number signifies the mean molecular weight of the PEG polymer). PEG400 was added to a concentration of 20% (v/v) to the yeast S100 extract while stirring at 18°C and incubated for 30 minutes. Precipitated proteins were removed by centrifugation at 30,000 x g for 30 minutes at 4°C. The supernatant was then precipitated by raising the concentration of PEG400 to 30% (v/v) as described above. The precipitate of this step, which contains FAS, was recovered by centrifugation at 30,000 x g for 30 minutes at 4°C and resuspended in purification buffer containing 2% (w/v) sucrose, 10 mM DTT and 0.01% (w/v) Lauryl Maltose Neopentyl Glycol (LMNG) in an orbital shaker at 18°C. The resuspended material was loaded on 10%–45% (w/v) linear sucrose gradients in purification buffer containing 10 mM DTT, which were centrifuged at 100,000 x g for 16 h at 4°C. Gradients were harvested in 1 mL fractions. SDS-PAGE was utilized to identify fractions containing FAS. Selected fractions were pooled and precipitated by the addition of 40% (v/v) PEG400. After centrifugation (30,000 x g, 30 minutes), the supernatant was removed and the precipitate was resuspended in purification buffer containing 2% (w/v) sucrose, 10 mM DTT and 0.01% (w/v) LMNG. The resuspended material was loaded on linear 10%–45% (w/v) sucrose gradients in purification buffer containing 10 mM DTT, and centrifuged at 79,000 x g for 16 h at 4°C. Fractions containing FAS were identified by SDS-PAGE, pooled and cycled in the presence of 50 μM Malonyl CoA and 100 μM of NADPH for 30 min at 18°C. The protein was precipitated and concentrated by the addition of 40% (v/v) PEG400 and resuspended in purification buffer containing 2% (w/v) sucrose, 10 mM DTT and 0.01% (w/v) LMNG. Another round of linear 10%–45% (w/v) sucrose gradients in purification buffer containing 10 mM DTT, centrifuged at 60,000 x g for 16 h at 4°C and subsequent re-precipitation of FAS fractions with 40% (v/v) PEG400 was required to yield a final purified protein preparation at ~15 mg/ml in purification buffer containing 10% sucrose (w/v), 10 mM DTT and 0.01% (w/v) LMNG. Protein concentrations were determined by Bradford assay (BioRad, Munich, Germany) using a BSA standard. This procedure reproducibly resulted in a yield of 15-20 mg purified yeast FAS.

Purification of the γ subunit

For γ subunit purification, 7 g of cells were resuspended in 42 mL of resuspension buffer (20 mM Tris-HCl pH 8.0, 500 mM NaCl, 10 mM imidazole, 0.2 mM PMSF, 10 mM benzamidine). After addition of 2 U/ml DNase and 0.33 mg/ml lysozyme, the suspension was incubated for 30 min at 4°C. Cells were lysed by passing twice through an Avestin Emulsiflex C3 fluidizer (Avestin, Mannheim, Germany) at 15,000 PSI. The obtained lysate was centrifuged (30 min, 50,000 g, 4°C) and filtered through Minisart NML Plus cellulose-acetate syringe filters with a 0.45 μm pore size (Sartorius). The cleared lysate was loaded onto a Ni-NTA gravity column (5 mL bed volume) pre-equilibrated with 20 column volumes (CV) of resuspension buffer. The column was washed with 20 CV resuspension buffer, followed by 20 CV of washing buffer (20 mM Tris-HCl pH 8.0, 500 mM NaCl, 20 mM imidazole, 0.2 mM PMSF, 10 mM benzamidine). For elution of the bound γ subunit, 5 CV of elution buffer (20 mM Tris-HCl pH 8.0, 500 mM NaCl, 500 mM imidazole, 0.2 mM PMSF, 10 mM benzamidine) were applied and collected in 2 mL fractions. The elution fractions were analyzed with SDS-PAGE, the γ subunit containing fractions pooled, and the protein concentration photometrically determined (MW = 17.4 kDa, ε_{280} = 5960).

To cleave the N-terminal His_6-TEV-tag, TEV-protease was added to the protein in an enzyme-to-protein ratio of 1:50 followed by dialysis overnight in 5 l dialysis buffer (20 mM Tris-HCl pH 8.0, 5 mM β-ME, 100 mM NaCl) at 4°C. The digested γ subunit was applied to a Ni-NTA column, which was pre-equlilibrated with 20 CV dialysis buffer. The flow-through was collected in 2 mL fractions and single fractions were analyzed by SDS-PAGE. Fractions containing pure γ subunit were pooled and concentrated to a final concentration of 20 mg/ml using a 10 kDa MWCO Amicon Ultra 15 centrifugal concentrator (Millipore). The final protein was aliquoted, frozen in liquid nitrogen and stored at −80°C.

For further kinetic and structural investigations, purified γ subunit was thawed and dialysed into the kinetic assay buffer (0.05 M BisTris pH 6.5, 0.05 M potassium acetate, 0.5 mM magnesium acetate) at 4°C using 6-8 kDa MWCO Dialyzer Mini D-Tubes (Millipore).

Salt concentration-dependent dissociation of the γ subunit

FAS/γ subunit complex (0.52 mg) was loaded on linear 10%–45% (w/v) sucrose gradients in purification buffer (0.05 M BisTris pH 6.5, 0.05 M potassium acetate, 0.01 M magnesium acetate) containing 10mM DTT supplemented with either 0, 100, or 200 mM KCl. The gradients were centrifuged at 120,000 x g for 16h at 4°C and were harvested in 200 μl fractions. All fractions of the gradients at the three salt concentrations were then analyzed by SDS-PAGE.

Binding affinity of the γ subunit to FAS

To determine the binding affinity of the γ subunit to the FAS, γ subunit was fluorescently labeled with NHS-Rhodamine (Thermo Fisher Scientific) according to the manufacturer's protocol, followed by passage through a desalting column to remove excess unreacted dye. Different concentrations of NHS-Rhodamine labeled γ subunit were added to 40 pmol Δγ-FAS in assay buffer (0.05 M BisTris pH 6.5, 0.05 M potassium acetate, 0.5 mM magnesium acetate) in a total reaction volume of 40 μl. The mix was incubated at 30°C for 30 minutes. 10 μl of each reaction mix were then loaded onto a 1.5% (w/v) agarose gel (in 0.5X TBE, 2 mM $MgCl_2$) and run at 75 mA for 2 hours at 4°C. The fluorescence signal from the FAS/γ subunit complex was imaged using an Amersham imager 600 (GE Healthcare) and quantified using the ImageJ software (Schindelin et al., 2012). Each data point was measured in triplicate and the mean and SD were calculated. The dissociation constant of the γ subunit was calculated using the Hill Equation 1, or, alternatively, using a quadratic Equation 2 described below.

$$F(\gamma-\text{subunit}) = F_0 + \frac{\Delta F_{\max}\cdot[\gamma-\text{subunit}]^n}{K_{0.5}^n + [\gamma-\text{subunit}]^n} \tag{1}$$

$$F(\gamma-\text{subunit}) = F_0 + \frac{\Delta F_{\max}}{2\cdot[\text{FAS}]}\cdot \left[\left([\gamma-\text{subunit}]+[\text{FAS}]+K_D^{\text{app}}\right) - \sqrt{\left([\gamma-\text{subunit}]+[\text{FAS}]+K_D^{\text{app}}\right)^2 - 4\cdot[\gamma-\text{subunit}]\cdot[\text{FAS}]}\,\right]\Bigg) \tag{2}$$

Where F_0 denotes the background fluorescence, DF_{max} the maximal amplitude of the fluorescent signal, $K_{0.5}$ or $K_D{}^{app}$ the dissociation constant of the binding equilibrium between FAS and the γ subunit, n the Hill coefficient as a measure of cooperativity (n = 1, no cooperativity; n > 1, positive cooperativity, n < 1, negative cooperativity), [γ subunit] the applied concentration of γ subunit and [FAS] the concentration of FAS at a per active-compartment basis, that is 6 compartments per FAS molecule.

Steady-state kinetics

Steady-state kinetics of FAS-catalyzed substrate turnover in the presence or absence of the γ subunit were analyzed spectrophotometrically (V-750 UV-Visible spectrophotometer, Jasco Instruments) in a continuous assay monitoring NADPH consumption at 340 nm and 30°C. Substrate concentration dependence was studied for all three native FAS substrates: acetyl-CoA, malonyl-CoA and NADPH. Prior to use, commercially purchased acetyl-CoA and malonyl-CoA substrates were further purified by Reversed-Phase (RP)-HPLC (ÄKTA BASIC 900, GE Healthcare Life Sciences) using a preparative column (Machery-Nagel Nucleodur® 100-5-C18, 250 mm x 21 mm, 5 μm, flow rate: 10 ml/min). UV-absorption was simultaneously detected at 215 nm, 260 nm and 280 nm, and elution was performed using a linear gradient from 100% A (water + 0.1% (v/v) TFA) to 100% B (79.9% acetonitrile (v/v) + 20% ddH2O + 0.1% (v/v) TFA). The peak fractions of the corresponding substrates were collected, lyophilized and stored at −80°C until use. Substrate concentrations were determined spectrophotometrically using the known molar extinction coefficients (NADPH: ε_{340} = 6220 M^{-1} cm^{-1}; acetyl-CoA: ε_{260} = 15400 $M^{-1}cm^{-1}$; malonyl-CoA: ε_{260} = 15400 $M^{-1}cm^{-1}$).

In order to analyze the concentration dependence for the substrate acetyl-CoA, the concentrations of malonyl-CoA (120 μM), and NADPH (320 μM) were kept constant and saturating, and acetyl-CoA concentrations were varied between 0-300 μM. In the case of malonyl-CoA, acetyl-CoA (180 μM) and NADPH (320 μM) were kept constant and saturating, and malonyl-CoA concentrations were varied between 0-240 μM. For the analysis of the concentration dependence of NADPH, acetyl-CoA (180 μM) and malonyl-CoA (120 μM) were kept constant and saturating, and NADPH concentrations were varied between 0-320 μM. All kinetic measurements were performed after pre-incubation of 0.254 μM FAS either with or without 127 μM of the γ subunit for a total of 30 min at 30°C. The final assay mixture contained 12.7 nM FAS in complex with or without 6.35 μM γ subunit, either 0.2 mg/ml trypsin inhibitor for non-crowding conditions or 20 mg/ml trypsin inhibitor as crowding conditions, kinetic assay buffer (0.05 M BisTris pH 6.5, 0.05 M potassium acetate, 0.5 mM magnesium acetate), the substrate concentrations indicated above, and 10% (*w/v*) sucrose. The reaction mix was incubated for 1 min at 30°C and the enzymatic reaction was then started by the addition of the substrate malonyl-CoA. Each data point was measured in triplicate and the mean and SD were calculated. In case of substrates acetyl-CoA and malonyl-CoA, we estimated the initial rates by linear regression of the absorbance changes at 340 nm between 0 and 5 s. In the case of co-substrate NADPH, we used Equation 3 that accounts for a time-dependent transition from a less active to a more active species:

$$A_{340}(t) = A_0 - \Delta ss \cdot t + \frac{\Delta ss - \Delta_0}{k_{\mathrm{obs}}} \cdot \left[1 - \exp^{(-k_{\mathrm{obs}} \cdot t)}\right] \tag{3}$$

Here, A_0 denotes the starting absorbance, Δss the absorbance change at steady-state (steady-state rate), Δ_0 the absorbance change at $t = 0$ (initial rate), and k_{obs} the first-order rate constant of activation. In order to reliably define the period of FAS activation, we routinely calculated the 1$^{\mathrm{st}}$ derivative for all progress curves allowing us to differentiate FAS activation from the onset of substrate depletion (see Figure S3).

Thus obtained initial and steady-state rates were analyzed using either the Hill equation (NADPH, Equation 4), or modified Hill equations taking into account substrate-excess inhibition as observed for acetyl-CoA and malonyl-CoA (Equations 5 and 6) (Müller et al., 2015):

$$v(S) = \frac{V_{\mathrm{max}} \cdot [S]^n}{K_{0.5}^n + [S]^n} \tag{4}$$

$$v(S) = \frac{V_{\mathrm{max}} \cdot [S]^n \cdot (K_{\mathrm{i}})}{K_{0.5}^n \cdot K_{\mathrm{i}} + [S]^n \cdot (K_{\mathrm{i}} + [S])} \tag{5}$$

$$v(S) = \frac{V_{\mathrm{max}} \cdot [S]^n \cdot (K_{\mathrm{i}} + \alpha \cdot [S])}{K_{0.5}^n \cdot K_{\mathrm{i}} + [S]^n \cdot (K_{\mathrm{i}} + [S])} \tag{6}$$

where $K_{0.5}$ denotes the substrate dissociation equilibrium constant, n the Hill coefficient ($n = 1$, no cooperativity; $n > 1$, positive cooperativity, $n < 1$, negative cooperativity), K_{i} the inhibitory substrate dissociation equilibrium constant, and α as a measure of the relative reactivity retained in the ternary complex of FAS with substrate and inhibitory substrate. In Equation 5, α is assumed to be zero, while it is non-zero in Equation 6.

Preparative reconstitution of the FAS/γ subunit complex

For reconstitution of the FAS/γ subunit complex, a 100-fold excess of the γ subunit was added to 4 μM Δγ-FAS and incubated at 30°C for 30 min. The protein was then loaded on 10%–45% (w/v) sucrose gradients in purification buffer containing 10 mM DTT, and then centrifuged at 64,000 x g for 16 h at 4°C to remove unbound excess γ subunit. Gradients were harvested in 400 μl fractions. We then used SDS-PAGE to identify fractions containing FAS/γ subunit complex. Selected fractions were pooled and precipitated by the addition of 40% (v/v) PEG400. After centrifugation (30,000 x g, 30 minutes), the supernatant was removed and the precipitate was resuspended in purification buffer containing 10% (w/v) sucrose, 10 mM DTT and 0.01% (w/v) LMNG to a final concentration of 10 mg/ml.

Cryo-EM sample preparation

EM grids were prepared using both Δγ-FAS and FAS/γ subunit complexes at a protein concentration of 0.5 mg/ml. The particles were adsorbed to a continuous carbon film attached to a Quantifoil (3,5/1) (Quantifoil, Jena, Germany) grid for 2 min at 4°C. The grid was then transferred to a Vitrobot Mark IV (Thermofisher, Germany) plunge-freezer, where it was vitrified after blotting for 8 s at 4°C and 100% humidity.

For γ subunit titration experiments, 1.5 mg/ml Δγ-FAS solution was used and recombinant, purified γ subunit was titrated in 0-, 2-, 6-, 24-, and 96-fold excess. The protein mix was incubated at 30°C for 30 min and then kept at 4°C. 4 μl of each sample was applied to freshly glow-discharged Quantifoil R1.2/1.3 holey carbon grids (Quantifoil Micro Tools, Jena, Germany) followed by plunge freezing as described above.

Cryo-EM data collection and image processing

Data were acquired on a Titan Krios (Thermo Fisher Scientific) operating at 300 kV using either a Falcon 3 (integrated mode) camera or a K2 summit (counting mode) camera (Gatan, Inc.). Data collection and processing statistics are summarized in Table S2. The acquired movies were motion corrected and dose weighted using Motioncor2 (Zheng et al., 2017) with all the frames split into

5X5 patches. The aligned frames were used to perform per micrograph CTF estimation using GCTF (Zhang, 2016). Particle selection was done using Gautomatch (from Dr. K. Zhang). All subsequent image processing steps were performed with Relion 3.0 (Scheres, 2012; Zivanov et al., 2018), unless otherwise specified (Figures S5 and S6). The extracted particles were subjected to 3 rounds of reference free 2D classification to remove bad/empty images. The remaining particles were refined with a mask around the central wheel using D3 symmetry. EMDB-1623 (Gipson et al., 2010) was low pass filtered to 30 Å and used as reference for all 3D refinement and 3D classification procedures. The refined particles were then classified without alignment, with a mask around the two domes. The conformation of the dome was consistent among the different classes obtained, however, it was well resolved only in one class which consisted of ~50%–60% of the particles used for classification. The particles from the 3D class displaying the best resolution were selected and used for one more round of 3D refinement and classification as performed before. The data further classified into 3 main classes. The particles belonging to their respective classes were refined resulting in structures with resolutions of 3.5 Å or below. Even though all the 3 classes were at comparable resolutions, their local resolutions, especially in the dome region of the molecule were very different. Only one class displayed high resolution details throughout the whole molecule. Finally, the particles belonging to this class were selected and used to perform CTF refinement (and particle polishing for the FAS/γ subunit complex dataset) followed by 3D refinement. The final refinement step was performed by applying different symmetries (C1-, C3- or D3 symmetry) to check for any structural artifacts that might be introduced due to the applied symmetry.

Energy Landscapes

The data were processed as described above until the first classification step. For this analysis, batches of ~100,000 particles were classified into 15 classes. The particles belonging to each class were selected and refined again without applying any masks. The refined 3D volumes from each dataset (a total of 165) were then used for the conformational landscape analysis as previously described (Haselbach et al., 2017, 2018). The 3D volumes were first aligned in USCF Chimera (Pettersen et al., 2004) with the central wheel of the molecule as the reference point. Further steps were performed in the COW software suite (https://www.cow-em.de). The 3D volumes were normalized and filtered to 20 Å. We then performed 3D Principle Component Analysis (PCA). The eigenvectors of the PCA hierarchically describe the major variance within the dataset and can be interpreted as the major modes of motion within the FAS molecules. The resultant eigenvectors representing the variance in the data were then used to describe each 3D volume using the following equation:

$$X_i = \overline{X} + \Sigma_{j=1}^{n} a_{i,j} e_i \tag{7}$$

, where every volume X_i is described as a linear combination of the average volume $\overline{X}$ and the eigenvectors e_i multiplied with the linear factor $a_{i,j}$. The first $(e_1)$and second (e_2)eigenvectors, which depict motions of compaction and rotation of the FAS dome, respectively, were selected for calculating conformational landscapes. The particle number belonging to each class was used to calculate their free energies as multiples of the Boltzmann factor $(k_B T)$:

$$\Delta\Delta G = k_B T \ln\left(\frac{p_i}{p_0}\right), \tag{8}$$

where T is the absolute temperature, k_B the Boltzmann constant, p_i is the number of particles in state i and p_0 is the number of particles in the most populated state. The linear factors of e_1 and e_2 calculated as per Equation 7 contributing to the input 3D volumes represent the x and y coordinates of the landscapes whereas the z axis represents the free energies of each class.

FAS Crystallization and Crystal Stabilization

$\Delta\gamma$-FAS in purification buffer containing 10% sucrose (w/v), 10 mM DTT and 0.01% (w/v) LMNG was crystallized at 7 mg/ml by mixing 1 µl protein + 1 µl crystallization buffer A (0.1 M HEPES pH 7.0, 0.3 M sodium-malonate pH 7.0, 11.5%–13% (w/v) PEG3350) in Crystalgen hanging drop diffusion plates (Jena Bioscience, Germany) over a 750 µl reservoir of crystallization buffer A. For the FAS/γ subunit complex, a 7-fold molar excess of γ subunit (in the buffer used for $\Delta\gamma$-FAS) was added to a 7 mg/ml protein solution of $\Delta\gamma$-FAS and incubated for 30 minutes at 30°C. The reconstituted complex was then crystallized by mixing 1 µl protein + 1 µl crystallization buffer B (0.1 M MES pH 6.2, 0.15-0.3 M ammonium sulfate, 7%–8% (w/v) PEG 8000) in Chryschem sitting drop vapor diffusion plates (Hampton Research, Aliso Viejo, USA) over a 500 µl reservoir of crystallization buffer B. The crystals took 3-7 days to grow at 18°C and were usually around 150 × 200 × 200 µm in size.

The crystals obtained were transferred to 4°C by gradually decreasing the temperature in a linear manner over 48 h using a Rumed® E100 incubator (Rubarth Apparate GmbH, Germany). Stabilization and dehydration procedures were performed as following: 1) The drop was unsealed and 2 µl of the reservoir solution was added to the drop. Then 2 µl of crystal stabilization buffer A (0.1 M HEPES pH 7.0, 0.3 M sodium malonate pH 7.0, 15% (w/v) PEG3350) for $\Delta\gamma$-FAS and stabilization buffer B (0.1 M MES pH 6.2, 0.3 M ammonium sulfate, 12% (w/v) PEG 8000) for the FAS/γ subunit complex was added. 2) 2 µl of the respective crystal stabilization buffer containing 5% (v/v) ethylene glycol was added followed by removal of 2 µl of solution from the drop. Then 2 µl of the respective crystal stabilization buffer containing 5% (v/v) ethylene glycol was again added to the drop. This procedure was repeated with the respective crystal stabilization buffer containing 10% and then 20% (v/v) ethylene glycol. 3) The reservoir solution was exchanged for the respective crystal stabilization buffer containing 25% (v/v) ethylene glycol and the drop was resealed. The crystals were then allowed to equilibrate by vapor diffusion in excess of 16 h.

X-ray Diffraction Data collection

The crystals were harvested in Spine Litholoops (Molecular Dimensions, Suffolk, UK or Jena Bioscience, Jena, Germany) mounted on magnetic pins, and vitrified by plunge-cooling in liquid nitrogen. The data were collected on EMBL beamline P14 at the PETRA III storage ring (DESY, Hamburg, Germany) using a MD3 vertical-spindle diffractometer (EMBL and Arinax, Moirans, France) and an EIGER 16M detector (Dectris, Baden, Switzerland). A white beam refractive lens transfocator and slits were used to obtain homogeneous X-ray beams which matched the crystal dimensions (Schrader et al., 2016). Diffraction data were scaled and integrated with the XDS program package (Kabsch, 2010).

X-ray structure determination

Initial phases for Δγ-FAS were determined by molecular replacement performed with MOLREP (Vagin and Teplyakov, 2010) using the *Saccharomyces cerevisiae* FAS structure (PDB ID: 2UV8) (Leibundgut et al., 2007). The model was built and optimized by several rounds of interactive manual model building in Coot (Emsley and Cowtan, 2004) and refinement in Refmac5 (Murshudov et al., 2011). Finally, TLS refinement was performed, where each TLS domain was defined by individual enzymatic domains. The obtained structure displays excellent stereochemistry with 19.7 % / 21.8% (R_{work}/R_{free}) (Table S2). Analysis of the diffraction data with the STARANISO server indicated mild anisotropy. This suggested anisotropic scaling and truncation of the data should allow for better refinement of the model. This was indeed the case and resulted in a final model with lower average B-factors and 19.2 % / 21.1 % (R_{work}/R_{free}; Table S2).

The refined Δγ-FAS crystal structure was used to determine the initial phases by molecular replacement with MOLREP (Vagin and Teplyakov, 2010) for the FAS/γ subunit complex diffraction data. The obtained density map was found to correlate better with the FAS/γ subunit complex model (as determined by cryo-EM) rather than the Δγ-FAS structure. Therefore, we used the model of α and β subunits from the FAS/γ subunit complex cryo-EM model in initial refinement of the X-ray data. Notably, the ACP domain and the γ subunit were removed from the structure prior to refinement to avoid introducing a phase bias. After several rounds of rigid body refinement in Refmac5 (Murshudov et al., 2011), difference densities corresponding to the ACP domain and γ subunit next to the AT and ER domain, respectively could be easily identified. The missing domains were then placed into their respective densities followed by additional rounds of refinement using Coot (Emsley and Cowtan, 2004) and Refmac5 (Murshudov et al., 2011). Owing to the resolution of the FAS/γ subunit complex structure, we have chosen to deposit the structure as a poly-Ala trace only.

Cryo-EM Model building

The crystallographic Δγ-FAS model was used as the initial model for both the Δγ-FAS and FAS/γ subunit complex structures determined by cryo-EM. It was docked into the EM densities as a rigid body using UCSF Chimera (Pettersen et al., 2004). An additional round of rigid body refinement was then performed in Refmac5 (Murshudov et al., 2011). The model then underwent several rounds of manual modeling in Coot (Emsley and Cowtan, 2004) and refinement in Refmac5 (Murshudov et al., 2011).

Models for the γ subunit were generated by interactive modeling based on side-chain densities in Coot (Emsley and Cowtan, 2004) and cross-validated models generated based on sequence homology using the Robetta prediction server (Kim et al., 2004). The model was additionally cross-validated using the cross-linking data. There were two unstructured regions (60-76, 114-132) of this protein that could not be confidently modeled.

For the final refinement and validation of the models, we used the maps reconstructed using D3 symmetry as they had the best resolution. Fourier shell correlation (FSC) between the refined model and the map was calculated (FSC_{sum}). The model was also refined using the first unfiltered half-map. This model was then compared to the first half map (FSC_{work}) as well as to the second half-map (FSC_{free}) to check for signs of overfitting. All figures were made using Pymol (Schrödinger, 2015), Chimera (Pettersen et al., 2004) and ChimeraX (Goddard et al., 2018).

Phosphorylation analysis of the γ subunit using Mass Spectrometry

Phosphorylated peptides were enriched following the EasyPhos (Humphrey et al., 2015) method with changes. In brief, peptides were resuspended in 1050 μL of 228 mM KCl, 3.9 mM KH2PO4, 38% ACN (v/v) and 4.5% TFA (v/v). For phosphopeptide enrichment, peptides were incubated with TiO2 beads for 20 min at 40°C at a beads-to-protein ratio of 10:1. Beads were washed three times with 60% ACN/1% TFA. Elution was performed twice with 40% ACN/3.75% NH4OH (v/v) on empty spin columns (Harvard Apparatus). Subsequently, the pH of the eluate was adjusted to 2 by adding TFA, dried and desalted by using C18 spin columns (Harvard apparatus).

Phosphorylated peptides were measured on a Q Exactive HF-X mass spectrometer (Thermo Fisher Scientific). MS1 resolution was set to 120,000, AGC target to 1×10^6, maximum IT to 50 ms. The 30 most abundant precursor ions were fragmented using HCD with an NCE of 30%. MS2 scans were acquired with a resolution of 30,000, an AGC target of 5×10^5 and a maximum IT of 128 ms. Dynamic exclusion was set to 45 s. The liquid chromatography gradient was similar to the one used for the cross-linked peptides but adapted to a 90 min method, starting with 10% B.

Raw files were analyzed by MaxQuant (v. 1.6.0.1) (Cox and Mann, 2008) with default settings and phosphorylation as variable modification on serines, threonines and tyrosines. Protein sequences of the FAS γ subunit were taken from UniProt and used as database. All phosphorylation sites that were identified for the γ subunit had a localization probability higher than 0.94.

Crosslinking Mass Spectrometry

We analyzed the purified FAS/γ subunit complex by crosslinking mass spectrometry. The protein complex was incubated with 1 mM of BS3 crosslinker (from a 100mM stock in DMSO) for 30 min at 30°C. The reaction was quenched with 100 mM Tris-HCl pH 8.0 (from a 1 M stock). Proteins were reduced and alkylated with 10 mM dithiothreitol and 40 mM iodoacetamide, respectively. In the presence of 1 M urea, proteins were digested by trypsin in an enzyme-to-protein ratio of 1:50 at 37°C overnight. Peptides were acidified with trifluoroacetic acid (TFA) added to a final concentration of 0.5% (v/v), desalted on MicroSpin Colums (Harvard Apparatus) following the manufacturer's instructions, and vacuum dried. Peptides were resuspended in 50 μL of 30% acetonitrile/0.1% (v/v) TFA before enriching of cross-linked species by peptide size exclusion (SuperdexPeptide 3.2/300 column, GE Healthcare). Fractions of 50 μL were collected and those that eluted first and contain the cross-linked peptide pairs were analyzed by LC-MS/MS.

Cross-linked peptides of the first replicate were measured in technical duplicates on an Orbitrap Fusion Lumos Tribrid Mass Spectrometer coupled to a Dionex UltiMate 3000 UHPLC system (both Thermo Fisher Scientific) equipped with an in-house-packed C_{18} column (ReproSil-Pur 120 C18-AQ, 1.9 μm pore size, 75 μm inner diameter, 30 cm length, Dr. Maisch GmbH). Samples were separated by applying the following gradient: mobile phase A consisted of 0.1% formic acid (v/v), mobile phase B of 80% acetonitrile/ 0.08% formic acid (v/v). The gradient started at 5% B, increasing to 12, 15 or 20% B within 3 min (according to fraction), followed by a continuous increase to 48% B within 45 min, then keeping B constant at 90% for 8 min. After each run the column was again equilibrated to 5% B for 2 min. The flow rate was set to 300 nL/min. MS1 survey scans were acquired in the orbitrap (OT) with a resolution of 120,000, an injection time (IT) of 60 ms and an automatic gain control (AGC) target of 5×10^5. Dynamic exclusion (DE) was set to 10 s and only charge states between 3 and 8 were considered for fragmentation. MS2 spectra were acquired in the OT of the 20 most abundant precursor ions, resolution 30,000, IT 120 ms and AGC target 5×10^4. Fragmentation was enforced by higher-energy collisional dissociation (HCD) at 30% normalized collision energy (NCE). The second replicate was treated with the following changes: we used a Q Exactive HF-X mass spectrometer (Thermo Fisher Scientific), at MS1 the IT was set to 50 ms and the AGC target to 1×10^6. At MS2, the IT was set to 128 ms and the AGC target to 1×10^5. DE covered 30 ms. Here, the 30 most abundant precursor ions were considered for fragmentation.

ProteomeDiscoverer 1.4 (Thermo Fisher Scientific) was used for converting.raw files into .mgf format (signal-to-noise ratio 1.5, 1000–10000 Da precursor mass). The generated .mgf files were subjected to pLink v. 1.23 (Yang et al., 2012) to identify cross-linked peptides. Here, default settings were applied with carbamidomethylation of cysteines as a fixed and oxidation of methionines as a variable modification, the FDR was set to 0.01. Spectra of inter-cross-links between FAS and the γ subunit within the first replicate were evaluated manually. For the second replicate, a score cut-off of 3 (-$\log_{10}$ transformation of the original pLink score) was applied and only cross-links supported by more than one cross-linked peptide spectrum match (CSMs) were considered.

QUANTIFICATION AND STATISTICAL ANALYSIS

Each data point to determine the binding affinity of the γ subunit and for the enzyme kinetics measurements in this paper were measured in triplicate. For binding affinity measurements, the fluorescence of FAS-bound γ subunit measured in agarose gels using an Amersham imager 600 and quantified using the ImageJ software (Schindelin et al., 2012). No data points were omitted. The mean and SD for n = 3 measurements per data point were calculated. In the case of enzyme kinetics triplicate measurements were individually used to determine the initial rates by linear regression of the absorbance changes using Sigmaplot (Systat Software Inc.), the mean and SD for n = 3 initial rates obtained in this manner at each data point were then calculated. No data points were omitted. The actual triplicate measurements to determine enzyme hysteresis are shown for one datapoint in Figure S2.

DATA AND CODE AVAILABILITY

The COW software is currently in an open beta test phase and can be downloaded from https://www.cow-em.de upon registration.

The coordinates for the determined structures are deposited in the Protein Data Bank (PDB accession codes 6QL5, 6QL6, 6QL7 and 6QL9). EM structures are deposited with the EMDB (accession codes 4577, 4578).

Supplemental Figures

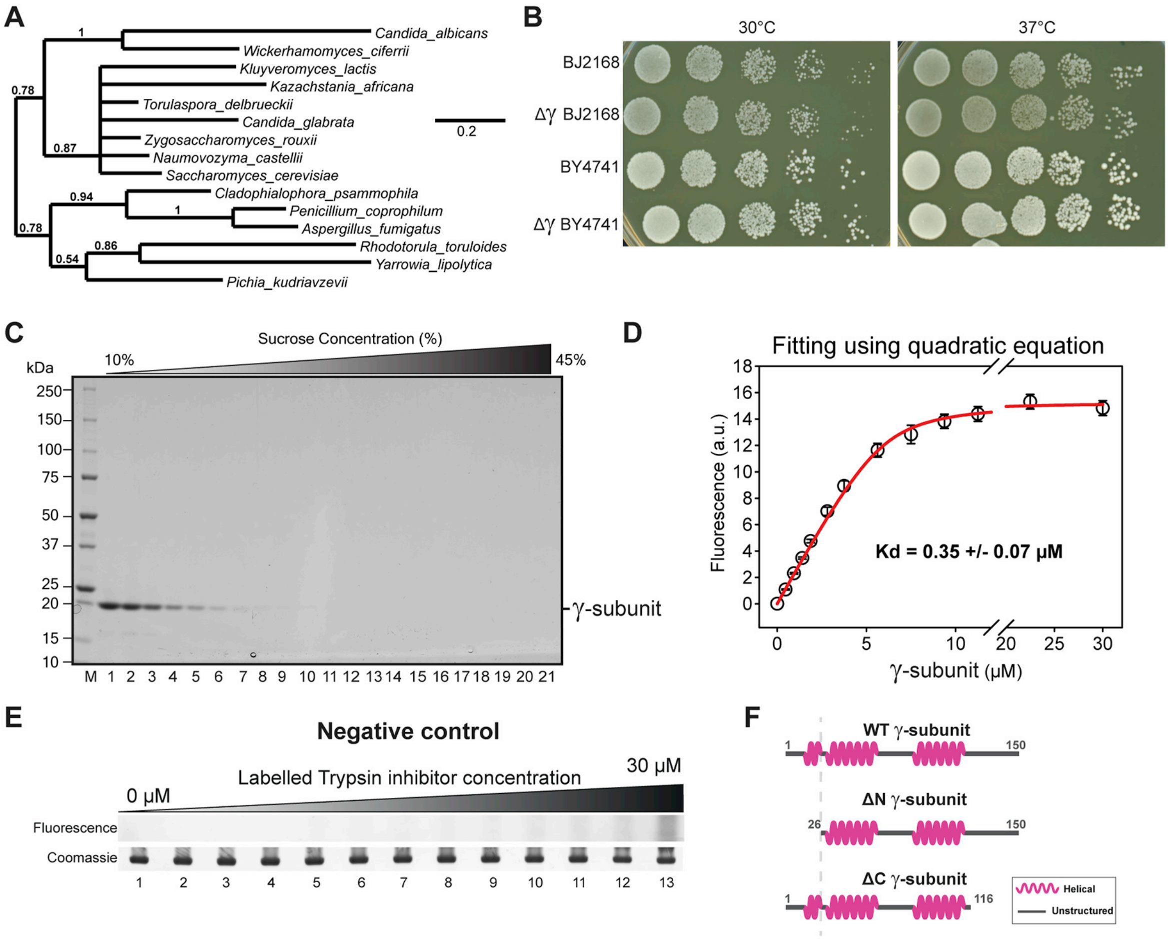

Figure S1. γ Subunit Is Conserved in Fungi and Specifically Interacts with FAS, Related to Figures 1 and 2

(A) Phylogenetic tree of *S. cerevisiae* FAS γ subunit homologs shown in the multiple sequence alignment in A). The phylogenetic tree was generated using "phylogeny.fr" webservice (Dereeper et al., 2008). Numbers at the branches indicate their bootstrap support values, whereas the scale bar represents the number of amino acid substitutions per site.

(B) Cells of the indicated genotype were spotted in 6-fold dilution and grown at the indicated temperature.

(C) Sedimentation behavior of isolated, recombinant γ subunit. SDS-PAGE analysis of sucrose density gradient fractions of recombinant γ subunit alone. The recombinant γ subunit protein is present in top fractions of the gradient and its sedimentation behavior is distinctly different from when it is bound to FAS in the 40S range. The dissociation of γ subunit from FAS at higher ionic strength (Figures 2A and 2B) leads to the same sedimentation behavior as that of isolated γ subunit shown here.

(D) Quantitative analysis of the fluorescence signal shown in Figure 2C fit with the quadratic Equation 2 (STAR Methods). The K_d of the γ subunit using such a model was 0.35 ± 0.07 μM. While the molar ratios employed in this binding experiment justify the use of a quadratic equation, note that a sigmoidal binding behavior, which is clearly visible in the raw data is not recapitulated by the quadratic equation. Nevertheless, fitting the data with both the Hill Equation 1 (STAR Methods) and the quadratic Equation 2 (STAR Methods) justify the conclusion that the γ subunit has a dissociation constant, which lies in the low micromolar range. Error bars represent SD.

(E) Negative control for the reconstitution of FAS with γ subunit. $\Delta\gamma$-FAS was titrated with fluorescently labeled trypsin inhibitor (a protein with a similar molecular weight and charge as the γ subunit). The top shows a fluorescence scan of the gel where FAS migrates to estimate binding to FAS, whereas the bottom depicts a Coomassie-stained native gel of the FAS region. No binding to FAS was observed, indicating that the Rhodamine dye alone does not promote binding to FAS and that the binding of the γ subunit is specific.

(F) Schematic representation of recombinant γ subunit constructs based on secondary structure predictions with a deletion of its N-terminal segment from residue 1 to 25 (ΔN γ subunit) or the C-terminal segment from residue 117 to150 (ΔC γ subunit) indicated.

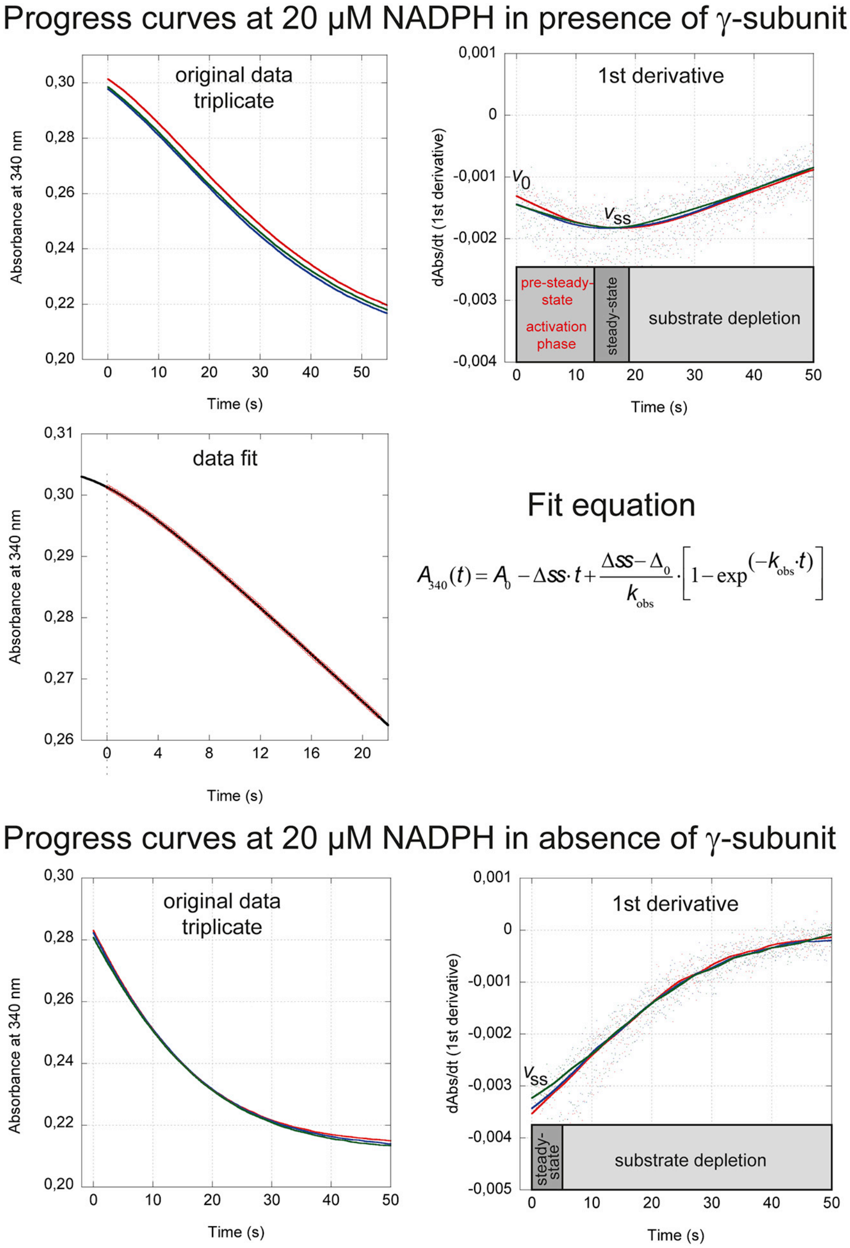

$$A_{340}(t) = A_0 - \Delta ss \cdot t + \frac{\Delta ss - \Delta_0}{k_{obs}} \cdot \left[1 - \exp^{(-k_{obs} \cdot t)}\right]$$

Figure S2. Hysteresis in FAS Turnover in the Presence of the γ Subunit, Related to Figure 3

Top panel: Shown are original data in triplicate of FAS turnover in the presence of the γ subunit at 20 μM NADPH (left) as well as the respective first derivatives (right) to determine pre-steady-state, steady-state and activation phases.

Middle panel: Quality of data fitting as indicated by the overlay of raw data (black line, left) with the fit (red line, left) obtained by the equation depicted in the right.

Bottom panel: Shown are original data in triplicate of FAS turnover in the absence of the γ subunit at 20 μM NADPH (left) as well as the respective first derivatives (right). Note that in this case no hysteresis is observed as indicated by the first derivative.

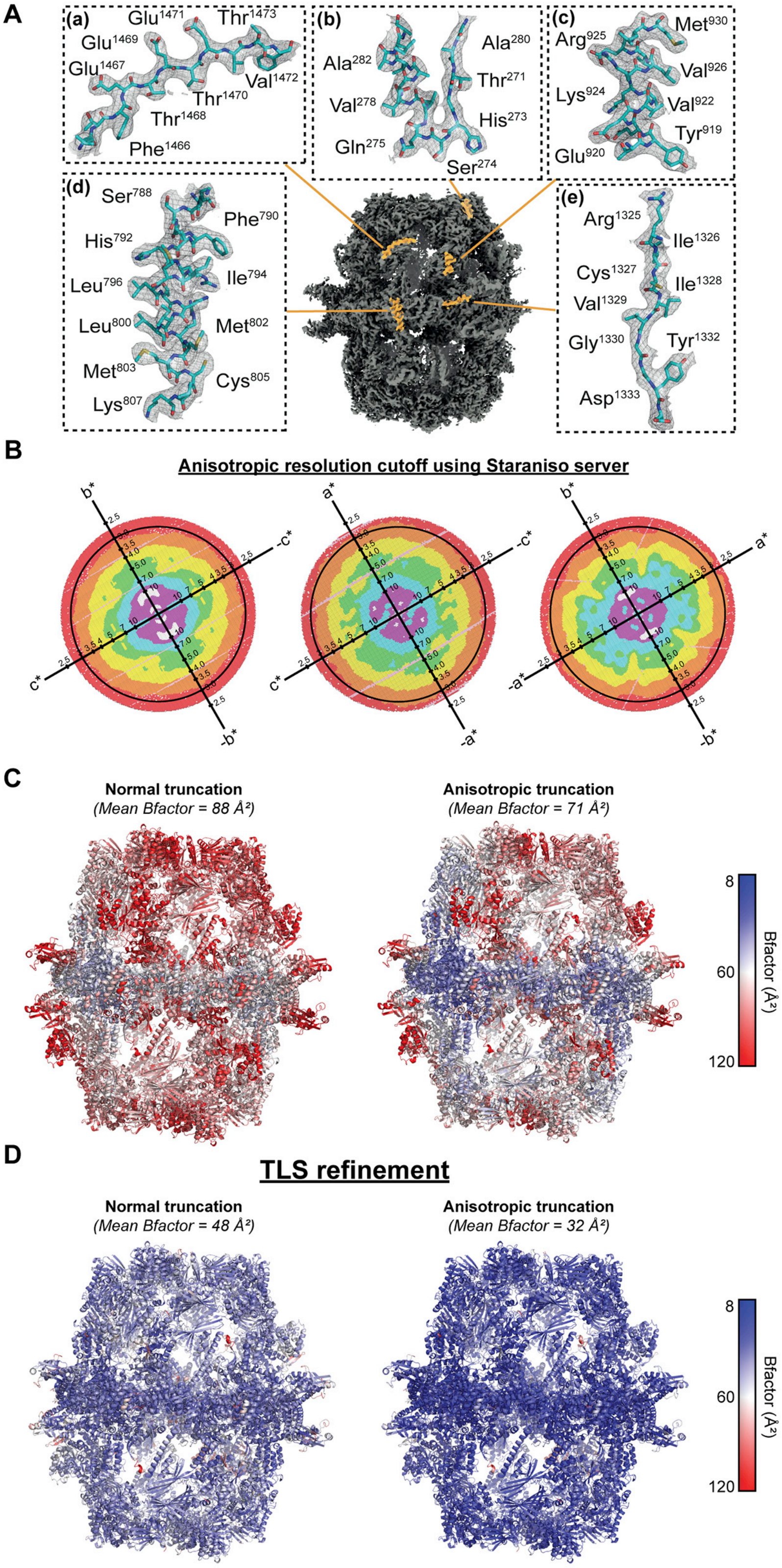

(legend on next page)

Figure S3. X-Ray Crystal Structure of Δγ-FAS, Related to Figure 4 and STAR Methods

(A) X-ray crystal structure of Δγ-FAS at 2.9 Å resolution. Several excerpts within the respective enzymatic domains displayed in ochre are utilized to show the quality of the final $2mF_o$-DF_c electron density maps contoured at: (a) DH domain 1.5 σ, (b) AT domain 1.5 σ, (c) ER domain 1.5 σ, (d) KR domain 2.0 σ and (e) KS domain 2.0 σ.

(B) Analysis of the Δγ-FAS X-ray dataset for anisotropic diffraction using the STARANISO server. Diffraction intensity plots along the three crystallographic axes. Note the strongest diffraction is along the a*-axis (2.8 Å), followed by the c*-axis (3.0 Å) and the weakest diffraction is along the b*-axis (3.1 Å). Since the crystal is nearly isometric in all three dimensions, this mild anisotropy is likely to represent the difference in unit cell numbers along the three crystallographic axes.

(C) B-factor distribution of main chain atoms of the refined Δγ-FAS model against data spherically truncated at 2.9 Å (left) and anisotropically truncated as indicated in (A) (right). A distinct drop in mean B-factors is visible upon anisotropic truncation of the data.

(D) B-factor distribution of main chain atoms of the Δγ-FAS model against data spherically truncated at 2.9 Å (left) and anisotropically truncated as indicated in (A) (right) after TLS refinement. TLS groups corresponded to individual enzymatic domains of the α- and β- subunits, respectively.

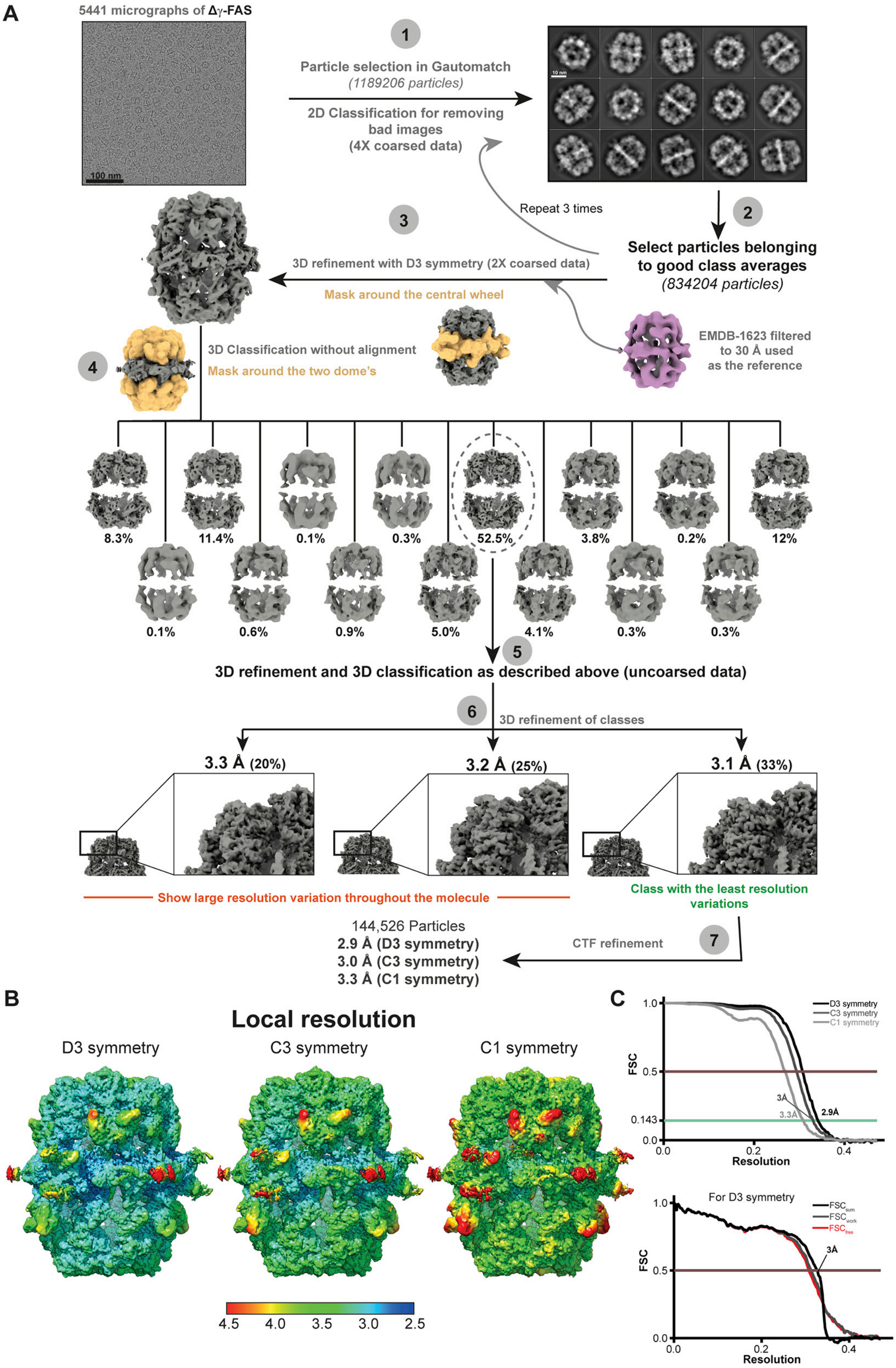

(legend on next page)

Figure S4. Scheme for Cryo-EM Data Processing for Δγ-FAS, Related to Figure 4 and STAR Methods

(A) The scheme depicts the different image processing steps performed.

(1) Motion-corrected and dose weighted micrographs were used for particle selection.

(2) Selected, individual particles were classified in 2D for 3 rounds, where particles belonging to bad classes (resulting from bad optical properties or low signal-to-noise) were removed after each step.

(3) The selected particles were then used for 3D refinement using D3 symmetry with the published cryo-EM structure of *Saccharomyces cerevisiae* FAS (EMDB – 1623) as a reference. During the 3D refinement, a mask was placed around the central wheel to focus the refinement around the most stable part of the protein.

(4) The alignment parameter of the particles from the previous step were used for classifying the particles into 15 classes. For classification, only the dome of the FAS was considered to sort out the major movements of this molecule.

(5) Particles from the best 3D class were selected followed by another round of 3D refinement and classification as described above.

(6) Particles from classes with resolutions below 4 Å after 3D classification were refined again.

(7) CTF refinement of particles belonging to the class with the most uniform resolution was performed followed by a final 3D refinement by applying different symmetries (C1-, C3- and D3 symmetry). The final 3D maps obtained had an overall resolution of 2.9 Å (D3 symmetry), 3.0 Å (C3 symmetry) and 3.3 Å (C1 symmetry).

(B) Local resolution map of the Δγ-FAS structure refined with different symmetries (C1-, C3-, or D3-symmetry). Each part of the density is colored according to the local resolution as specified in the color bar. The resolution range depicted is from 2.5 Å (blue) to 4.5 Å (red). The majority of the structure with D3 symmetry has local resolution varying from 2.5 Å to 3.5 Å.

(C) Fourier shell correlation (FSC) for the Δγ-FAS structures with different symmetric refinements (left) and FSC_{sum} (black), FSC_{work} (gray), as well as FSC_{free} (red) curves for validation of the model refined against the structure calculated with D3 symmetry (right) are shown.

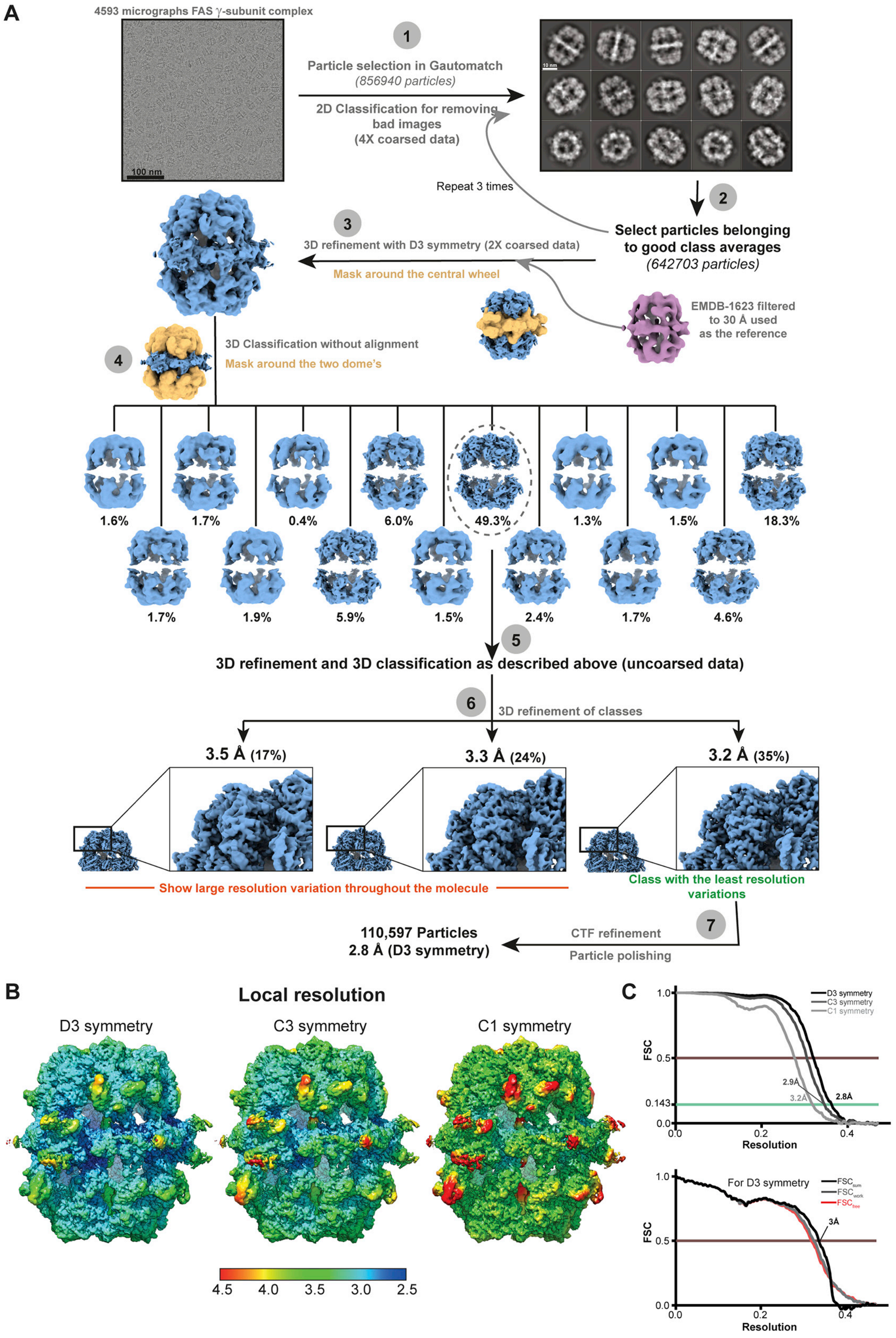

(legend on next page)

Figure S5. Scheme for Cryo-EM Data Processing for FAS/γ Subunit Complex, Related to Figures 4 and 5 and STAR Methods

(A) The scheme depicts the different image processing steps performed. The processing pipeline was identical to the one used for Δγ-FAS complex. For this dataset, after CTF refinement, particle polishing was performed in Relion for the particles used in the final 3D refinement step. The final 3D maps obtained for this complex had an overall resolution of 2.9 Å (D3 symmetry), 3.0 Å (C3 symmetry) and 3.3 Å (C1 symmetry).

(B) Local resolution map of the FAS/γ subunit complex structure refined with different symmetries (C1-, C3-, or D3-symmetry). Each part of the density is colored according to the local resolution as specified in the color bar. The resolution range depicted is from 2.5 Å (blue) to 4.5 Å (red). The majority of the structure with D3 symmetry has local resolution varying from 2.5 Å to 3.5 Å.

(C) Fourier shell correlation (FSC) for the FAS/γ subunit complex structures with different symmetric refinements (left) and $\mathrm{FSC}_{\mathrm{sum}}$ (black), $\mathrm{FSC}_{\mathrm{work}}$ (gray), as well as $\mathrm{FSC}_{\mathrm{free}}$ (red) curves for validation of the model refined against the structure calculated with D3 symmetry (right) are shown.

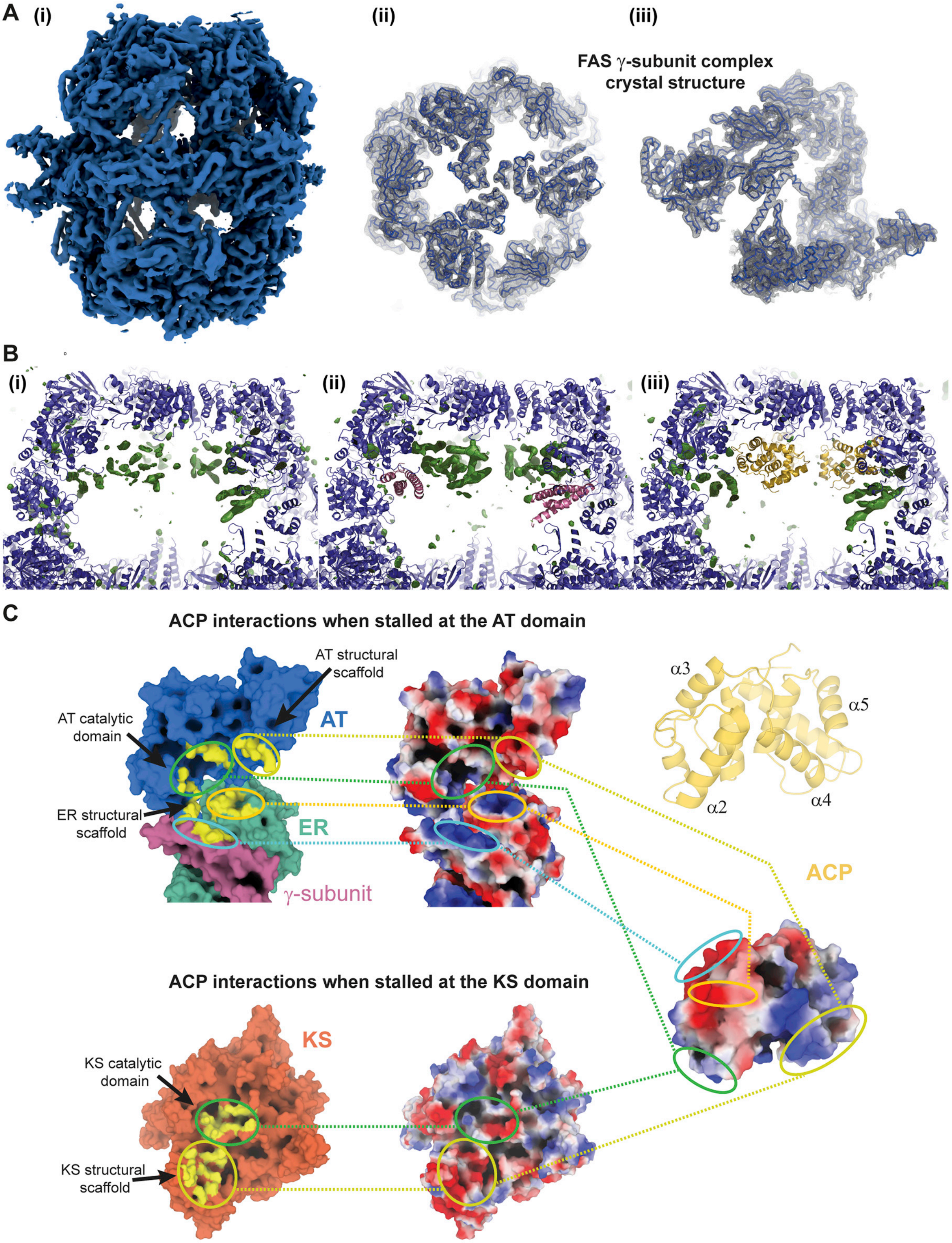

Figure S6. Crystallographic Structure of the Reconstituted FAS/γ Subunit Complex and Comparison of ACP Interactions at the AT and KS Domain, Related to Figures 4 and 5 and STAR Methods

(A) X-ray crystal structure of the FAS/γ subunit complex at 4.6 Å resolution. (a) Electron density of the entire FAS/γ subunit complex as an envelope colored in blue. Also depicted are top (b) and side view (c) of the Cα-trace models with their corresponding $2mF_o$-DF_c electron densities contoured at 1.5 σ.

(legend continued on next page)

(B) Difference density and omit maps for the location of ACP domains and γ subunits in the crystallographic FAS/γ subunit complex structure.

(i) Shown is the initial positive mF_o-DF_c difference density (green) contoured at 3 σ obtained, when only α and β subunit models are used for refinement of the 4.6 Å FAS/γ subunit complex crystallographic data. Densities corresponding to α-helical segments of ACP domain and γ subunit were observed next to the AT and ER domains, respectively. Their positions are identical to the ACP and γ subunit densities in the FAS/γ subunit complex cryo-EM structure.

(ii) ACP domain-omit mF_o-DF_c map is shown contoured at 3 σ to verify the correct modeling of this domain in the FAS/γ subunit complex.

(iii) A γ subunit omit mF_o-DF_c map is shown contoured at 3 σ to verify the correct modeling of this domain in the FAS/γ subunit complex.

(C) The interactions made by the ACP domain (yellow) when residing at the AT active site (top left) and KS active site (bottom left) are depicted using yellow coloring of density envelopes. Electrostatic potentials of the respective domains are presented in the central panel. The secondary structure of the ACP domain (top right) and its corresponding electrostatic potential (bottom right) are used to compare the interaction surfaces, when bound to the AT and KS domains, respectively. The ACP domain makes multiple contacts, when bound to the AT domain. Helix $\alpha2$ contacts residues near the active site channel, whereas helix $\alpha4$ and $\alpha5$ contact the structural scaffold of the AT domain (corresponding to the N-terminal residues of the β subunit). These same regions of the ACP domain are involved in interactions when the ACP domain is bound to the KS domain. Additionally, when bound to the AT domain, the loop between helix $\alpha2$ and $\alpha3$ contacts the ER domains, whereas in the presence of the γ subunit, the helix $\alpha3$ lies adjacent to the γ subunit. All ACP domain interactions with the respective FAS catalytic modules appear to rely on charge complementarity and thus electrostatic interaction.

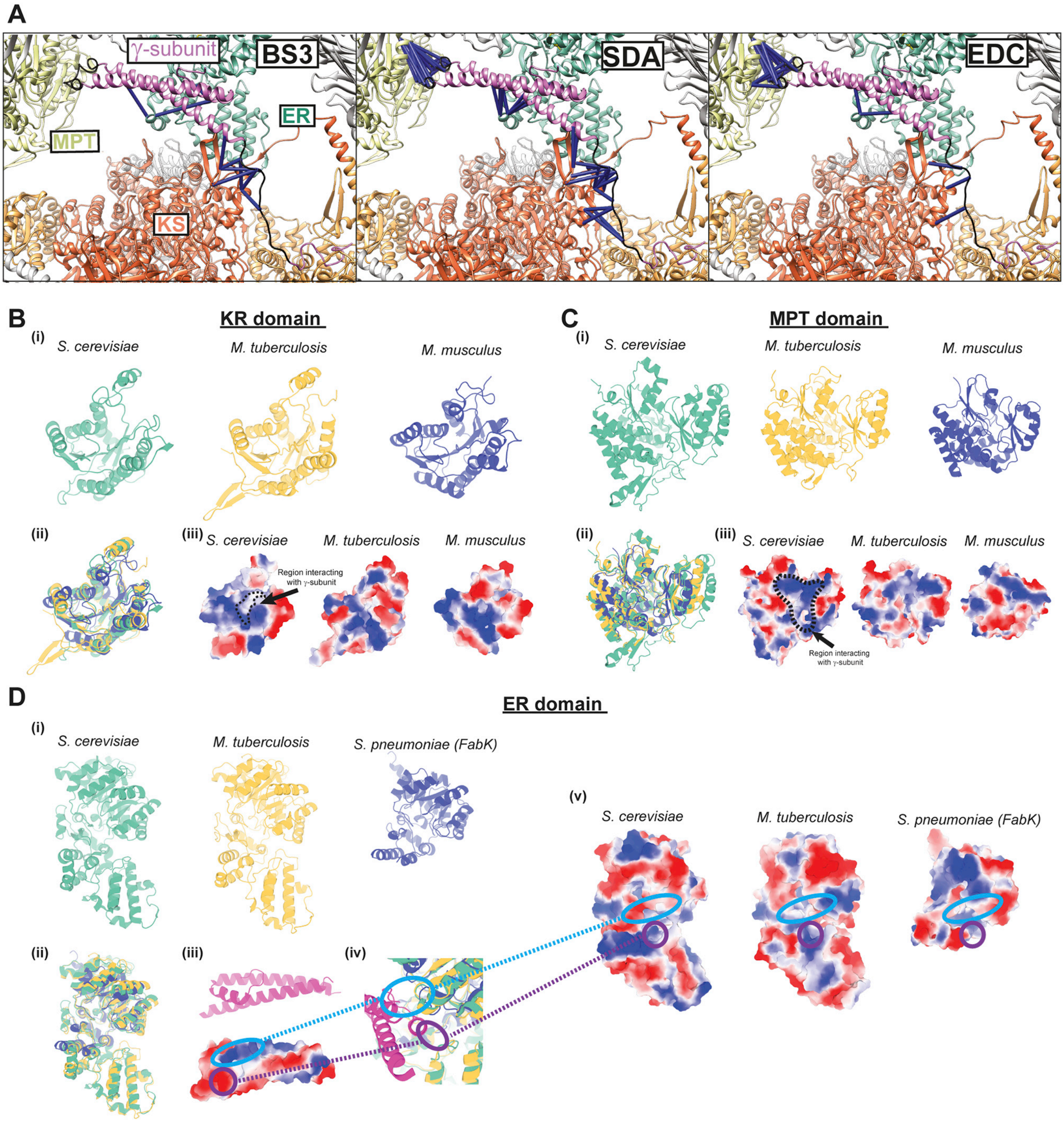

Figure S7. XL-MS Validation of the γ Subunit Model and Conservation of KR, MPT, and ER Domain Architecture among Different Type I FAS Systems, Related to Figure 5 and STAR Methods

(A) Crosslinks mapped on the final FAS/γ subunit complex structure for BS3 (left), SDA (middle) and EDC (right) are shown. The crosslinks are indicated by the blue rods. Only the crosslinks between residues within the distance threshold of 20 Å for the modeled part of the γ subunit and 30 Å for the un-modeled part of the γ subunit are depicted.

(B) KR domain

(i) KR domains of the *S. cerevisiae* (left), *M. tuberculosis* (middle) and *M. musculus* (right) type I FAS systems are depicted. This domain has a characteristic Rossmann-fold and is structurally conserved among the different organisms.

(ii) Overlay of the three KR domains.

(legend continued on next page)

(iii) Electrostatic representation of the respective KR domains. The charge distribution in the NADPH binding cleft (this region also binds the C terminus of the yeast FAS γ subunit) is very comparable among these different organisms.

(C) MPT domain

(i) MPT domains of the *S. cerevisiae* (left), *M. tuberculosis* (middle) and *M. musculus* (right) type I FAS systems are depicted. This domain is structural conserved among the different organisms.

(ii) Overlay of the three MPT domains.

(iii) Electrostatic representation of the respective MPT domains. The charge distribution outside the malonyl-CoA binding cleft (this region also binds the aspartate rich loop of the yeast FAS γ subunit) is very comparable among these different organisms.

(D) ER domain

(i) ER domains of the type I FAS systems from *S. cerevisiae* (left), *M. tuberculosis* (middle) and type II FAS system from *S. pneumoniae* (right) are depicted. This domain has a characteristic TIM barrel fold and is structurally conserved among the different organisms.

(ii) Overlay of the three ER domains.

(iii) The regions that are involved in binding the γ subunit by the yeast FAS (left) are also structurally similar in *M. tuberculosis* as well as in *S. pneumoniae*.

(iv) Electrostatic representation of the respective ER domains. the charge distribution on these different ER domains differ significantly suggesting that if a FAS γ subunit exists in these organisms, it would have a distinctly different sequence than that found in fungi.